

Towards information storage by designing both electron and hole detrapping processes in bismuth and lanthanide-doped $\text{LiRE}(\text{Si},\text{Ge})\text{O}_4$ (RE = Y, Lu) with high charge carrier storage capacity

Lyu, Tianshuai; Dorenbos, Pieter

DOI

[10.1016/j.cej.2020.124776](https://doi.org/10.1016/j.cej.2020.124776)

Publication date

2020

Document Version

Final published version

Published in

Chemical Engineering Journal

Citation (APA)

Lyu, T., & Dorenbos, P. (2020). Towards information storage by designing both electron and hole detrapping processes in bismuth and lanthanide-doped $\text{LiRE}(\text{Si},\text{Ge})\text{O}_4$ (RE = Y, Lu) with high charge carrier storage capacity. *Chemical Engineering Journal*, 400, Article 124776. ⁴
<https://doi.org/10.1016/j.cej.2020.124776>

Important note

To cite this publication, please use the final published version (if applicable).
Please check the document version above.

Copyright

Other than for strictly personal use, it is not permitted to download, forward or distribute the text or part of it, without the consent of the author(s) and/or copyright holder(s), unless the work is under an open content license such as Creative Commons.

Takedown policy

Please contact us and provide details if you believe this document breaches copyrights.
We will remove access to the work immediately and investigate your claim.



Towards information storage by designing both electron and hole detrapping processes in bismuth and lanthanide-doped LiRE(Si,Ge)O₄ (RE = Y, Lu) with high charge carrier storage capacity

Tianshuai Lyu*, Pieter Dorenbos

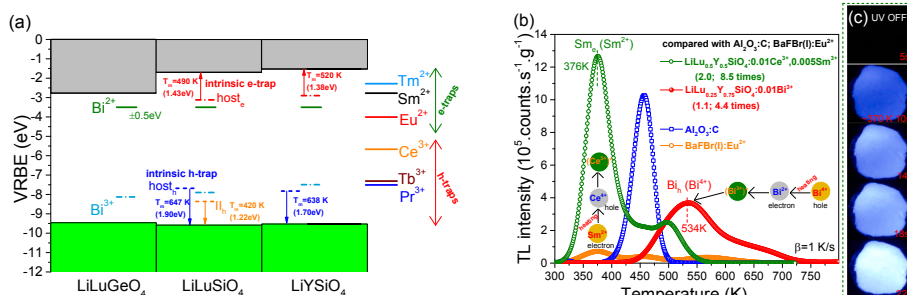
Delft University of Technology, Faculty of Applied Sciences, Department of Radiation Science and Technology, Section Luminescence Materials, Mekelweg 15, 2629JB Delft, the Netherlands



HIGHLIGHTS

- Rational design of new Ce³⁺ and Bi³⁺ storage phosphors for energy storage.
- Excellent Ce³⁺ and Bi³⁺ storage phosphors were discovered.
- Fully control of trap depth by both CB and VB engineering.
- New mechanism of hole liberation from Bi⁴⁺ and recombination with Bi²⁺.
- New insight of deep understanding storage phosphor mechanisms.

GRAPHICAL ABSTRACT



ARTICLE INFO

Keywords:

Energy conversion
Energy storage
Bismuth
Hole liberation
Trap engineering

ABSTRACT

Guided by vacuum referred binding energy (VRBE) diagrams, both the trapping and detrapping processes of electrons and holes are explored in the bismuth and lanthanide-doped LiRE(Si,Ge)O₄ (RE = Y, Lu) family of compounds. The Tm³⁺ electron trap has been combined with the deep hole traps of Ln³⁺ (Ln = Ce, Tb, or Pr) or Bi³⁺ in LiLuSiO₄. During the thermoluminescence readout, the electrons released from Tm²⁺ recombine with holes at Ln⁴⁺ and Bi⁴⁺ to produce typical Ln³⁺ 4f-4f or 5d-4f emission and Bi³⁺ A-band emission. The electron trap depth of lanthanide ions can be tuned by the choice of Ln³⁺ (Ln = Tm or Sm), and for fixed pair of Ln³⁺ and/or Bi³⁺ dopants like in LiLu_{1-x}Y_xSiO₄:0.01Ce³⁺, 0.01Ln³⁺ and LiLu_{1-x}Y_xSiO₄:0.01Bi³⁺, 0.01Sm³⁺ solid solutions, by adjusting x, resulting in the engineering of the VRBE at the conduction band bottom. The thermoluminescence (TL) intensity of the optimized LiLu_{0.5}Y_{0.5}SiO₄:0.01Ce³⁺, 0.005Sm³⁺ is about 8.5 times higher than that of the commercial X-ray BaFBr(I):Eu²⁺ storage phosphor. By combining deep Eu³⁺ or Bi³⁺ electron traps with Ln³⁺ (Ln = Tb or Pr) or Bi³⁺, Ln³⁺ and Bi³⁺ appear to act as less deep hole capturing centres in LiLuSiO₄. Here the recombination is achieved through hole liberation rather than the more commonly reported electron liberation. The holes are released from Ln⁴⁺ and Bi⁴⁺ to recombine with electrons at Eu²⁺ or Bi²⁺ to give characteristic Eu³⁺ 4f-4f and Bi³⁺ A-band emissions. The tailoring of Ln³⁺ and Bi³⁺ hole trap depths by crystal composition modulation is discussed in LiLu_{1-x}Y_xSiO₄ and LiLu_{0.25}Y_{0.75}Si_{1-y}Ge_yO₄:0.01Bi³⁺ solid solutions. The TL intensity of the optimized LiLu_{0.25}Y_{0.75}SiO₄:0.01Bi³⁺ is ~4.4 times higher than that of the commercial BaFBr(I):Eu²⁺. Proof-of-concept information storage will be demonstrated with X-ray or UV-light charged LiLu_{0.5}Y_{0.5}SiO₄:0.01Ce³⁺, 0.01Sm³⁺ and LiLu_{0.25}Y_{0.75}SiO₄:0.01Bi³⁺ phosphors dispersed in silicone gel imaging plates.

* Corresponding author.

E-mail address: T.lyu-1@tudelft.nl (T. Lyu).

<https://doi.org/10.1016/j.cej.2020.124776>

Received 16 February 2020; Received in revised form 13 March 2020; Accepted 14 March 2020

Available online 15 March 2020

1385-8947/© 2020 The Authors. Published by Elsevier B.V. This is an open access article under the CC BY license (<http://creativecommons.org/licenses/by/4.0/>).

1. Introduction

Charge carrier trapping processes have attracted attention for rational design of afterglow and storage phosphors and from a theoretical point of view [1,2]. The electron capturing and liberation processes have been widely studied for afterglow phosphors [3–8]. Korthout et al. reported the valence change of Eu^{2+} in the commercial afterglow phosphor $\text{SrAl}_2\text{O}_4:\text{Eu}^{2+},\text{Dy}^{3+}$ utilizing X-ray absorption near-edge spectroscopy (XANES) [9]. A partial oxidation of Eu^{2+} to Eu^{3+} appears after exposing the phosphor to X-rays. A valence state change of Dy^{3+} was not detected although it does play a role in the electron trapping process. Eu^{2+} is proposed to be an electron donor and the electrons liberated by photoionization migrate freely in the conduction band (CB) to be trapped by the electron capturing centre(s). A similar partial oxidation of Ce^{3+} to Ce^{4+} and a reduction of Cr^{3+} to Cr^{2+} appears in $\text{Y}_3\text{Al}_2\text{Ga}_3\text{O}_{12}:\text{Ce}^{3+},\text{Cr}^{3+}$ afterglow phosphor by XANES [10]. Here Ce^{3+} is the electron donor and Cr^{3+} acts as the electron acceptor.

Holes can also be released to recombine with an electron capturing centre through the valence band (VB) or by a migrating V_k centre [2,11]. Hole detrapping processes are rarely reported. In 1988, Chakrabarti et al. reported that Sm^{3+} is a recombination centre and Ce^{3+} is a hole capturing centre in $\text{MgS}:\text{Ce}^{3+},\text{Sm}^{3+}$ [12]. The holes are liberated from Ce^{4+} to recombine with electrons trapped at Sm^{2+} to give typical 4f-4f emission of Sm^{3+} . The other three examples are from recent studies on afterglow phosphors by Lyu et al. on REPO_4 [13–15] and Luo et al. on $\text{Gd}_{1-x}\text{La}_x\text{AlO}_3$ [2] and $\text{RE}_2\text{O}_2\text{S}$ [11] where hole detrapping processes from Bi^{4+} , Tb^{4+} , or Pr^{4+} were identified in REPO_4 and $\text{Gd}_{1-x}\text{La}_x\text{AlO}_3$. For $\text{RE}_2\text{O}_2\text{S}$, a hole detrapping process resulting in Ti^{4+} charge transfer emission is observed. There are rare reports on good storage phosphors discussing the hole-capturing and detrapping processes.

Bi^{3+} is a famous activator for photonic materials which is widely investigated [16]. However, Bi^{3+} doped storage phosphors are rarely reported and only a few Bi^{3+} -activated persistent luminescence phosphors have appeared up to now [14,17]. The trapping and detrapping processes regarding bismuth are complex and often remain unclear. A recent study on Bi^{3+} -doped REPO_4 indicates that Bi^{3+} not only can act as an electron trapping centre but also as a hole capturing centre [14]. More studies are required to unravel the charge carrier detrapping processes regarding bismuth to obtain more insights for rational design of bismuth activated storage phosphors.

Methods have been established to derive the energy level locations of the dopants like Cr^{2+} , Cr^{3+} , Bi^{2+} , Bi^{3+} , and divalent and trivalent lanthanides within the band gap of inorganic compounds [5,18–21]. Based on experimental spectroscopy, a vacuum referred binding energy (VRBE) diagram with host band and impurity energy level locations could be established to guide the exploration of charge carrier trapping materials [22]. Knowledge on the VRBE in dopant levels provides a tool to predict the trapping depths and determine what dopant may capture an electron and what dopant may capture a hole, which helps to explain and even adjust carrier trapping processes. The VRBE-aided methodology is so far mainly used in lanthanide and/or transition metal activated garnet compounds [3,23] and other oxide compounds like $\text{Ca}_3\text{Si}_2\text{O}_7$ [24] and Sr_2SiO_5 [25,26] to develop persistent luminescence phosphors. To the best of our knowledge, the VRBE-guided exploration of bismuth and/or lanthanide doped storage phosphors is rarely reported up to now.

The research on optical data storage is of interest because of the challenges for storage of fast-growing amount of data [27–34]. Storage phosphors are information storage materials which trap electrons and holes in host related defect traps after absorbing ionizing radiation [35–40]. They have been applied as storage media in information

storage applications [41–46], like digital dental radiographic imaging facility [47] and computed radiography (CR) based on an X-ray storage phosphor plate [45]. Today $\text{BaFBr}(\text{I}):\text{Eu}^{2+}$ is the widely utilized commercial X-ray storage phosphor [45,48]. Nevertheless, it is hygroscopic which limits its long-term durability after exposure in air. Scientists are exploring better storage phosphors in various crystals like $\text{BaCl}_2:\text{Eu}^{2+}$ [49], $\text{CsBr}:\text{Eu}^{2+}$ [50,51], and Lu_2O_3 [52]. Sidorenko et al. [53] reported the storage properties of $\text{LiLnSiO}_4:\text{Ce}^{3+},\text{Sm}^{3+}$ ($\text{Ln} = \text{Y}$ or Lu). After charging LiLuSiO_4 , Sm^{2+} liberates electrons already near room temperature (RT) resulting in strong fading of stored information. Situation is better in LiYSiO_4 with the Sm^{2+} TL glow peak near 390 K but a low density of the host material makes it less suited for application as X-ray storage phosphor. Recently, Dobrowolska et al. [35,54] reported excellent storage capacity of optimized $\text{LiLuSiO}_4:\text{Ce}^{3+},\text{Tm}^{3+}$. Its thermoluminescence (TL) intensity is about 4 times higher than that of commercial $\text{BaFBr}(\text{I}):\text{Eu}^{2+}$ storage phosphor after β irradiation. However, this phosphor was developed by a trial-and-error approach. The nature of the trap(s) and the role of thulium codoping in $\text{LiLuSiO}_4:\text{Ce},\text{Tm}$ are still unclear. This finding motivated a deeper study into the family of related compounds LiLuSiO_4 , LiLuGeO_4 , and solid solutions $\text{NaLu}_{1-x}\text{Y}_x\text{GeO}_4$ in Ref. [55] with using other dopants like Bi^{3+} and Eu^{3+} .

The spectroscopy of Bi^{3+} in LiYSiO_4 and LiLuSiO_4 and their solid solutions was already discussed in Ref. [55]. Also the spectroscopy of the lanthanides in these compounds is well known and with that information the VRBE schemes with all the relevant levels in the band gap were constructed in the Ref. [55]. In this work, with the knowledge and VRBE diagrams from in Ref. [55], we return to the silicate solid solutions of the family of LiLuSiO_4 , LiYSiO_4 , and LiLuGeO_4 . Here the focus is on 1) the engineering aspects of storage and afterglow phosphors and 2) developing and optimizing phosphors for application. Crystal composition modulation and dopant combinations using Bi^{3+} , Pr^{3+} , Tb^{3+} , Ce^{3+} , Tm^{3+} , or Sm^{3+} are explored with the aim to engineer either the recombination centre, the dominant glow peak temperature, or to optimize the afterglow or storage performance.

The VRBE diagram known for LiLuSiO_4 is shown in Fig. 1a) [55]. The VRBE of an electron at the ground states of divalent and trivalent lanthanides is linked by two zigzag curves a and b. The VRBE in the ground states of Bi^{3+} and Bi^{2+} is also provided. Fig. 1a) illustrates that Tm^{3+} , Sm^{3+} , Bi^{3+} , and Eu^{3+} act as ~ 0.62 , ~ 1.08 , $\sim 1.81 \pm 0.5$, and ~ 2.34 eV deep electron capturing centres, while Ce^{3+} , Pr^{3+} , Tb^{3+} , and Bi^{3+} act as ~ 3.89 , ~ 2.04 , ~ 2.22 , and ~ 1.90 eV deep hole capturing centres.

For afterglow phosphor application at RT, shallow trap depth ($< \sim 1$ eV) is required. For storage phosphor application at RT, deep trap depth ($> \sim 1$ eV) is needed. Fig. 1a) guides us to choose a proper combination of electron and hole trapping centres to engineer an electron or hole release process for a specific application. It was demonstrated that one may combine a deep hole trap like Ce, Pr, Tb, or Bi with a less deep electron trap like Tm or Sm to arrive at recombination at the hole trap generating either Ce, Tb, Pr, or Bi emission. One may also combine a hole trap like Pr, Tb, or Bi with a deeper electron trap like Eu or Bi to arrive at recombination at the electron trap leading to Eu or Bi emission. For instance, red Eu^{3+} 4f-4f emission may appear for the $\text{Eu}^{3+}\text{-Bi}^{3+}$ or $\text{Eu}^{3+}\text{-Tb}^{3+}$ pairs in LiLuSiO_4 when a hole is liberated from Bi^{4+} or Tb^{4+} to recombine with electrons at Eu^{2+} because Bi^{3+} and Tb^{3+} may act as less deep hole traps than the electron trap depth on Eu. By making solid solutions like $\text{LiLu}_{1-x}\text{Y}_x\text{SiO}_4$, $\text{LiLuSi}_{1-y}\text{Ge}_y\text{O}_4$, or $\text{LiLu}_{1-x}\text{Y}_x\text{Si}_{1-y}\text{Ge}_y\text{O}_4$, the VB-top and CB-bottom may be shifted up or down as predicted in the stacked VRBE scheme in Fig. 1b), leading to ~ 100 K shift of the temperature of glow peak maxima. Herewith one may tune the trap depth.

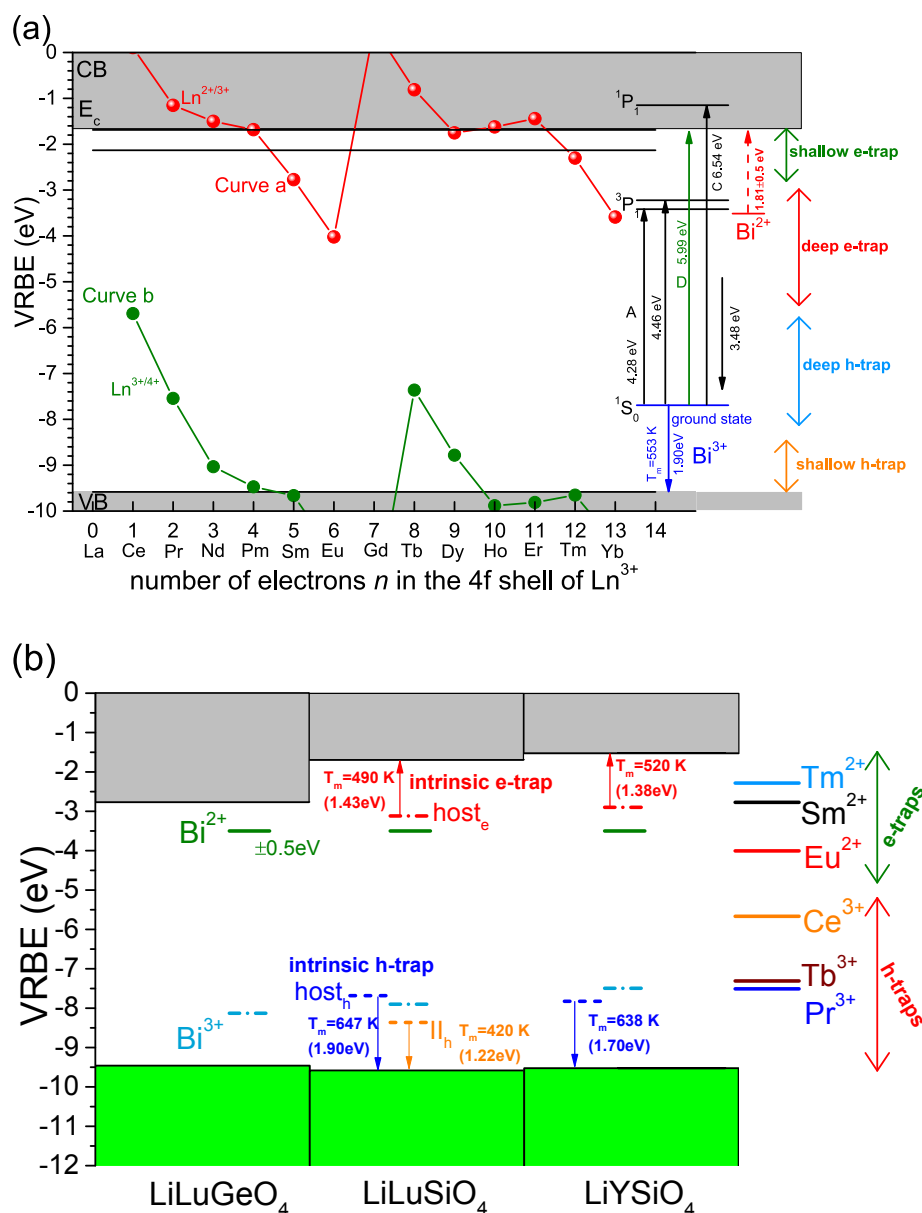


Fig. 1. Vacuum referred binding energy (VRBE) diagram for (a) LiLuSiO₄ and (b) stacked VRBE scheme for LiLuSiO₄ related family of compounds showing the VRBE in the ground states of Bi²⁺, Bi³⁺, and lanthanides. Experimentally observed transitions are denoted by arrows. The TL glow peaks II_n in Fig. 3(a), and host_e in Fig. 5(b) are used to determine the energy level locations of the intrinsic e-traps and h-traps in Fig. 1(b).

2. Experimental

Lanthanides and/or bismuth activated LiLu_{1-x}Y_xSiO₄ and LiLu_{0.25}Y_{0.75}Si_{1-y}Ge_yO₄ compounds were synthesized using a high-temperature solid-state reaction method. 0.2–0.7 mm SiO₂ (99.99%) crystals were purchased from Umicore company and then milled to small crystals. The other starting reagents were purchased from Sigma-Aldrich and used without further treatment. To compensate for the volatilization of lithium at high temperature, an excess of 10% Li⁺ above the stoichiometry ratio was used. The appropriate chemicals of rare earth oxides with high purity (99.99%), SiO₂ (99.99%), Li₂CO₃ (99.99%), Bi₂O₃ (99.999%), and GeO₂ (99.99%) were mixed well by adding acetone. The obtained mixture (~0.6 g) was placed in a corundum crucible and then fired at 800 °C for 8 h and at 1150 °C for 15 h in ambient atmosphere. For the compounds without bismuth doping, the mixture was further heated at 1170 °C for 5 h under an atmosphere of H₂/N₂ (H₂: N₂ 7%: 93%). To optimize the charge carrier storage capacity for LiLu_{0.25}Y_{0.75}SiO₄:0.01Bi³⁺ solid solution,

the starting mixture was first fired at 800 °C for 8 h and then at 1200 °C for 24 h under ambient atmosphere. The optimized LiLu_{0.5}Y_{0.5}SiO₄:0.01Ce³⁺, 0.005Sm³⁺ was synthesized at 800 °C for 2 h and then at 1170 °C for 10 h under an atmosphere of H₂/N₂ (H₂: N₂ 7%: 93%) for 3 times in a tube furnace. The utilized heating rate for the furnace is 3 °C/min. The obtained crystals were naturally cooled down to room temperature (RT) and ground to fine powders before further measurements.

The synthesized crystal structure was checked by an X-ray diffraction facility (PANalytical XPert PRO) using cobalt K α radiation ($\lambda = 0.178901$ nm) at 45 kV and 40 mA. For the temperature-dependent XRD patterns for LiLu_{0.25}Y_{0.75}Si_{1-y}Ge_yO₄:0.01Bi³⁺ ($y = 0.25$), another facility using copper K α 1 radiation ($\lambda = 0.154060$ nm) and a temperature-tailorable sample holder were utilized. The photoluminescence emission (PL) and PL excitation (PLE) spectra were recorded using a facility that contains a UV/VIS branch utilizing a Horiba Gemini 180 monochromator and a Newport 66921 Xe lamp and a VUV/UV branch with an ARC VM502 vacuum monochromator and a water-

cooled deuterium lamp. The emission from samples was recorded with a PerkinElmer MP-1993 photomultiplier. The excitation spectra were corrected by the wavelength-dependent lamp intensity. The Ce^{3+} and Bi^{3+} fluorescence decay curves were collected by the above facility which further connects with a waveform digitizer module and a pulsed YAG:Nd laser source (NT230-100-SH/DUV-SCU) that contains an optical parametric oscillator (OPO). The laser pulse repetition rate is 100 Hz and the pulse duration is 2–5 ns.

High-temperature thermoluminescence (TL) glow curves ranging from ~ 300 to 900 K were recorded using a facility which is composed of a RISØ TL/OSL reader (model DA-15), a DA-20 controller, and an EMI 9635QA photomultiplier tube. Prior to the TL measurement, the compounds were heated in the dark at a heating rate of 5 K/s from RT to ~ 900 K to empty the randomly trapped charge carriers and then cooled to room temperature. This was repeated 2 times more. The compounds were then charged by β -ray irradiation from a $^{90}\text{Sr}/^{90}\text{Y}$ source at a dose rate of ~ 0.7 mGy/s in nitrogen gas atmosphere.

Low-temperature TL (LTTL) glow curves were measured with a facility which contains a $^{90}\text{Sr}/^{90}\text{Y}$ β -ray source with a dose rate of ~ 0.4 mGy/s and a Perkin-Elmer channel photomultiplier tube (MP-1393) photon detector. Prior to the LTTL measurements, the compounds were pressed into pills with mass < 10 mg and then heated to 450 K for 180 s to liberate the randomly captured charge carriers under vacuum in the dark. The compounds were cooled to 90 K using liquid nitrogen and then irradiated with β irradiation. A 600 nm bandpass filter of 600FS40-50 (Andover Corporation) was placed between the compounds and the photomultiplier to select the Pr^{3+} or Eu^{3+} red emission. 350, 400, and 550 nm bandpass filters of 350FS40-50, 400FS40-50, and 550FS40-50 were utilized to select the characteristic ultraviolet Bi^{3+} , blue Ce^{3+} , and green Tb^{3+} emissions, respectively. For the TL intensity comparison of the synthesized compounds in this work with the commercial BaFBr(I): Eu^{2+} storage phosphor and an $\text{Al}_2\text{O}_3:\text{C}$ crystal chip, a 300–700 nm bandpass filter of Schott BG-39 was used. The TL intensities were corrected by the sample mass and β irradiation time and then expressed in counts/s/g.

To identify the emission centres during TL readout, thermoluminescence emission (TLEM) spectra were recorded on a setup which combines the RISØ TL/OSL reader and a UV/vis QE65000 (Ocean Optics) spectrometer. Prior to the TLEM measurements, the compounds

were heated to ~ 900 K to empty all traps and then cooled to room temperature followed by γ -ray charging in the dark using a ^{60}Co source. The TLEM plots measured by QE65000 at a heating rate of 1 K/s were corrected by the wavelength-dependent quantum efficiency of QE65000.

Prior to recording thermoluminescence excitation (TLE) spectra, compounds were heated to ~ 723 K to empty all traps and cooled to RT. The compounds were then illuminated during 800 s by monochromatic photons from a setup that is composed of a monochromator (Oriel Cornerstone 130) and a 150 W xenon arc lamp (Hamamatsu L2273). This setup has a wavelength resolution of 0.8 nm against 0.1 mm slit width. In this work, a 1 mm slit width was used. The setup is programmed by LabVIEW to automatically collect the TL glow curves from RT to ~ 723 K when the illumination wavelength ranged from 200 to 400 nm with steps of 10 nm. A TLE plot like in Fig. 7d) was established by integrating TL glow peaks and displaying integrated intensity against the illumination wavelength [11,56]. The measured TL intensities were corrected by the illumination time, compound mass, and the xenon lamp intensities as a function of wavelength. A filter was placed between the compounds and the photomultiplier tube to select the Ce^{3+} or Bi^{3+} characteristic emission.

To compare the readout speed of stored information in storage phosphors, the TL glow curves after β -ray charging followed by photon stimulation were recorded on the above RISØ TL/OSL reader, which further connects a 475 nm blue LED or a wavelength-tailored laser beam produced from the NT230-100-SH/DUV-SCU facility. The scanning electron microscope (SEM) images and the energy-dispersive X-ray spectroscopy (EDX) mapping for solid solutions $\text{LiLu}_{0.5}\text{Y}_{0.5}\text{SiO}_4:0.01\text{Ce}^{3+}, 0.01\text{Sm}^{3+}$, $\text{LiLu}_{0.25}\text{Y}_{0.75}\text{SiO}_4:0.01\text{Bi}^{3+}$, and $\text{LiLu}_{0.25}\text{Y}_{0.75}\text{Si}_{0.75}\text{Ge}_{0.25}\text{O}_4:0.01\text{Bi}^{3+}$ were measured by using JEOL JSM-IT100 facility. A 254 nm Hg lamp and an UV-lamp with the main emission near 365 nm were used to charge the $\text{LiLu}_{0.5}\text{Y}_{0.5}\text{SiO}_4:0.01\text{Ce}^{3+}, 0.01\text{Sm}^{3+}$ storage phosphor. An iPhone 8Plus was utilized to take the photographs for Ce^{3+} related emission. For the $\text{LiLu}_{0.5}\text{Y}_{0.5}\text{SiO}_4:0.01\text{Ce}^{3+}, 0.01\text{Sm}^{3+}$ dispersed in silicone film, the silicone gel was mixed well with an appropriate amount of storage phosphor to form a gel film on a glass substrate. The film was placed in a vacuum for 300 s to remove air bubbles and then put in air at RT for 10 h.

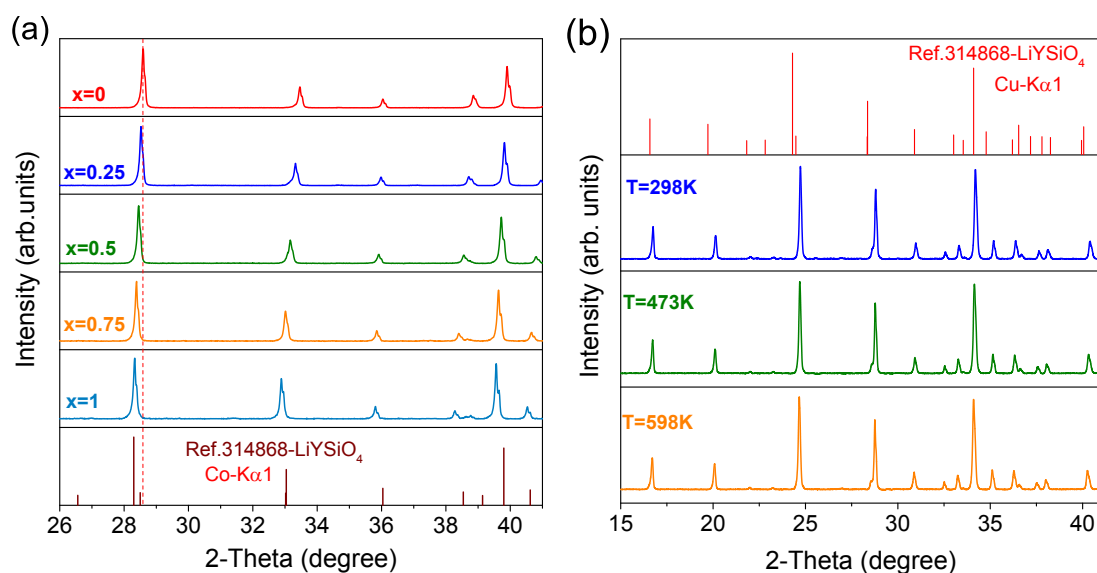


Fig. 2. XRD patterns of (a) $\text{LiLu}_{1-x}\text{Y}_x\text{SiO}_4:0.01\text{Ce}^{3+}, 0.01\text{Sm}^{3+}$ ($x = 0-1$) recorded at RT, and (b) $\text{LiLu}_{0.25}\text{Y}_{0.75}\text{Si}_{1-y}\text{Ge}_y\text{O}_4:0.01\text{Bi}^{3+}$ ($y = 0.25$) solid solution recorded at 298, 473, and 598 K.

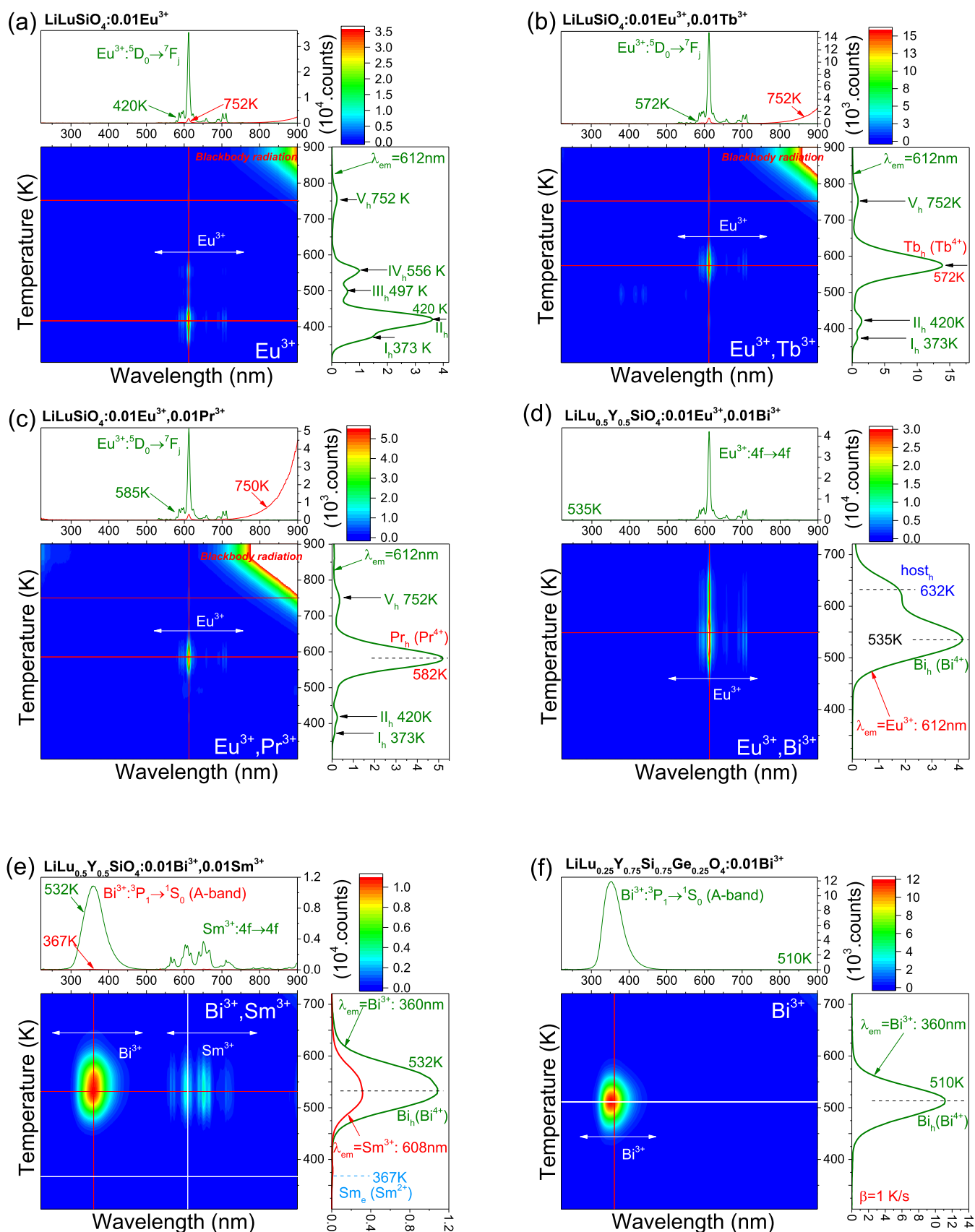


Fig. 3. TL emission (TLEM) plots for (a) $\text{LiLuSiO}_4:0.01\text{Eu}^{3+}$, (b) $\text{LiLuSiO}_4:0.01\text{Eu}^{3+},0.01\text{Tb}^{3+}$, (c) $\text{LiLuSiO}_4:0.01\text{Eu}^{3+},0.01\text{Pr}^{3+}$, (d) $\text{LiLu}_{0.5}\text{Y}_{0.5}\text{SiO}_4:0.01\text{Eu}^{3+},0.01\text{Bi}^{3+}$, (e) $\text{LiLu}_{0.5}\text{Y}_{0.5}\text{SiO}_4:0.01\text{Bi}^{3+},0.01\text{Sm}^{3+}$, and (f) double solid solution $\text{LiLu}_{0.25}\text{Y}_{0.75}\text{Si}_{0.75}\text{Ge}_{0.25}\text{O}_4:0.01\text{Bi}^{3+}$ recorded at a heating rate of 1 K/s after γ -ray irradiation.

3. Results

3.1. X-ray diffraction patterns for solid solutions

The X-ray diffraction (XRD) patterns for $\text{LiLu}_{1-x}\text{Y}_x\text{SiO}_4:0.01\text{Ce}^{3+},0.01\text{Sm}^{3+}$ ($x = 0-1$) with different content of yttrium are shown in Fig. 2a). With increasing x , the XRD peaks slightly shift towards smaller 2θ angles. This confirms that the yttrium cations enter the lutetium site and increase the cell volume because yttrium has a larger ionic radius than lutetium. The patterns evidence that solid solutions appear in the prepared crystals of $\text{LiLu}_{1-x}\text{Y}_x\text{SiO}_4:0.01\text{Ce}^{3+},0.01\text{Sm}^{3+}$ in Fig. 2a), and for $\text{LiLu}_{0.25}\text{Y}_{0.75}\text{Si}_{1-y}\text{Ge}_y\text{O}_4:0.01\text{Bi}^{3+}$ the same in Fig. S2.

Fig. 2b) shows the XRD patterns for the double solid solution $\text{LiLu}_{0.25}\text{Y}_{0.75}\text{Si}_{1-y}\text{Ge}_y\text{O}_4:0.01\text{Bi}^{3+}$ ($y = 0.25$). Impurity phases or structural change are absent when the solid solution was heated from 298 to 598 K.

3.2. Engineering hole liberation from Tb^{4+} , Pr^{4+} , and Bi^{4+} in $\text{LiLu}_{1-x}\text{Y}_x\text{SiO}_4$ solid solutions

TL emission (TLEM) studies were carried out to identify the

recombination centres in Ln^{3+} and/or Bi^{3+} doped $\text{LiLu}_{1-x}\text{Y}_x\text{SiO}_4$ in Fig. 3. Additional TLEM spectra for other $\text{LiLu}_{1-x}\text{Y}_x\text{Si}_{1-y}\text{Ge}_y\text{O}_4$ phosphors with other combinations of Ln^{3+} doping or different yttrium or germanium content can be found in Figs. S3–S5 and S14.

For $\text{LiLuSiO}_4:0.01\text{Eu}^{3+}$ in Fig. 3a), TL peaks near 373, 420, 497, 556, and 752 K with characteristic Eu^{3+} 4f-4f red emission emerge, that will be referred to as peaks I_h , II_h , III_h , IV_h , and V_h , respectively. Upon co-doping Tb^{3+} in $\text{LiLuSiO}_4:0.01\text{Eu}^{3+},0.01\text{Tb}^{3+}$ in Fig. 3b), a broad and intense TL peak near 572 K named Tb_h (Tb^{4+}), that will be attributed to hole release from Tb^{4+} , appears while monitoring the Eu^{3+} red emission. The similar applies to Pr^{3+} co-doping in $\text{LiLuSiO}_4:0.01\text{Eu}^{3+},0.01\text{Pr}^{3+}$ in Fig. 3c) where a TL peak near 582 K named Pr_h (Pr^{4+}) emerges.

Replacing Tb^{3+} or Pr^{3+} by the hole trapping centre of Bi^{3+} , again characteristic Eu^{3+} 4f-4f emission appears in $\text{LiLu}_{0.5}\text{Y}_{0.5}\text{SiO}_4:0.01\text{Eu}^{3+},0.01\text{Bi}^{3+}$ with TL glow peaks near 535 and 632 K in Fig. 3d). Fig. 3e) shows the TLEM plot for $\text{LiLu}_{0.5}\text{Y}_{0.5}\text{SiO}_4:0.01\text{Bi}^{3+},0.01\text{Sm}^{3+}$ where Sm^{3+} acts as a less deep electron trap than Bi^{3+} and Eu^{3+} . Broad Bi^{3+} A-band emission peaking at ~ 360 nm with a weak TL peak near 367 K named peak Sm_e , that will be assigned to electron liberation from Sm^{2+} , and a broad TL glow peak (Bi_h) ranging from 425 to 700 K and peaking near 532 K emerges. The

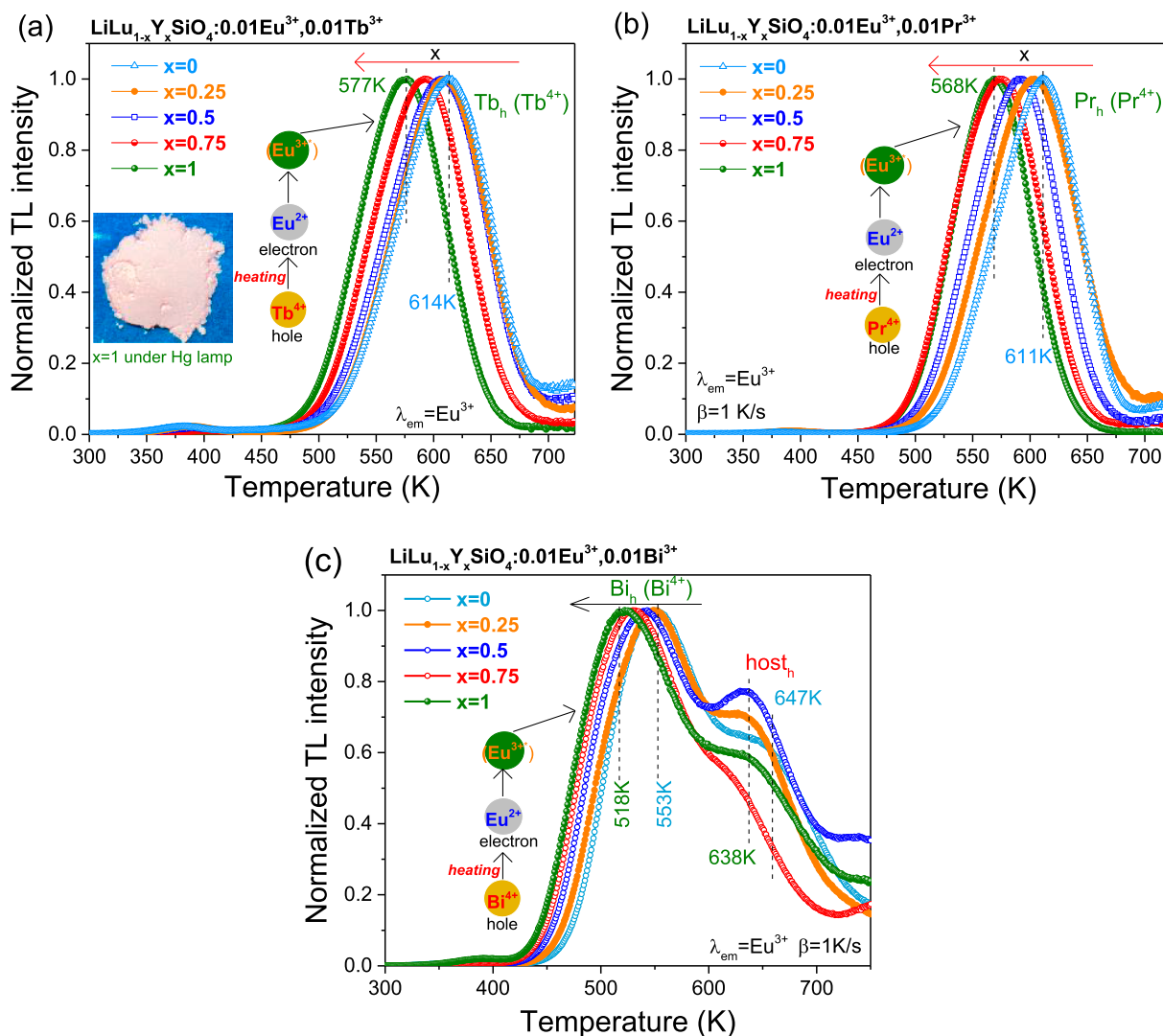


Fig. 4. Normalized TL glow curves for (a) $\text{LiLu}_{1-x}\text{Y}_x\text{SiO}_4:0.01\text{Eu}^{3+},0.01\text{Tb}^{3+}$, (b) $\text{LiLu}_{1-x}\text{Y}_x\text{SiO}_4:0.01\text{Eu}^{3+},0.01\text{Pr}^{3+}$, and (c) $\text{LiLu}_{1-x}\text{Y}_x\text{SiO}_4:0.01\text{Eu}^{3+},0.01\text{Bi}^{3+}$ solid solutions while monitoring the Eu^{3+} red emission recorded at a heating of 1 K/s after β irradiation. The inset in a) shows a photograph of $\text{LiYSiO}_4:0.01\text{Eu}^{3+},0.01\text{Tb}^{3+}$ under Hg lamp illumination. (For interpretation of the references to colour in this figure legend, the reader is referred to the web version of this article.)

~532 K TL peak is also observed in $\text{LiLu}_{0.5}\text{Y}_{0.5}\text{SiO}_4:0.01\text{Eu}^{3+},0.01\text{Bi}^{3+}$ in Fig. 3d), which will be attributed to hole liberation from Bi^{4+} . Note that not only characteristic Bi^{3+} A-band emission but also typical Sm^{3+} red 4f-4f emission appears in Fig. 3e). It is ascribed to an energy transfer process from Bi^{3+} to Sm^{3+} because the TL glow curves in Fig. 3e) share the same shape when selecting the Bi^{3+} A-band emission or when selecting the Sm^{3+} 4f-4f emission. This applies also for $\text{LiLu}_{1-x}\text{Y}_x\text{SiO}_4:0.01\text{Bi}^{3+},0.01\text{Sm}^{3+}$ with $x = 0.25$ and 0.75 in Fig. S14b)-c). The energy transfer from Bi^{3+} to Sm^{3+} is further evidenced by photoluminescence excitation spectra of $\text{LiYSiO}_4:0.01\text{Bi}^{3+},0.01\text{Sm}^{3+}$ in Fig. S19c). Like in Fig. 3d)-e), a Bi_h (Bi^{4+}) TL peak near 510 K appears in the TL emission plot for the double solid solution $\text{LiLu}_{0.25}\text{Y}_{0.75}\text{SiO}_4:0.01\text{Bi}^{3+}$ in Fig. 3f).

Fig. 1b) shows that the VRBE in the valence band top of LiYSiO_4 is about 0.1 eV higher than that of LiLuSiO_4 . Because the VRBEs in the ground states of lanthanides are almost invariant, it implies that the temperature of a TL glow peak due to hole liberation from Tb^{4+} or Pr^{4+} should decrease. Ln^{3+} and/or Bi^{3+} doped $\text{LiLu}_{1-x}\text{Y}_x\text{SiO}_4$ crystals were synthesized to further study and explore such hole trapping process.

Fig. 4a) shows the normalized TL glow curves for

$\text{LiLu}_{1-x}\text{Y}_x\text{SiO}_4:0.01\text{Eu}^{3+},0.01\text{Tb}^{3+}$ solid solutions after β irradiation. The as recorded TL glow curves are shown in Fig. S8a). With increasing x , the Tb_h (Tb^{4+}) TL glow peak near 614 K shifts about 37 K towards lower temperature, confirming the above prediction. The same applies to $\text{LiLu}_{1-x}\text{Y}_x\text{SiO}_4:0.01\text{Eu}^{3+},0.01\text{Pr}^{3+}$ solid solutions as shown in Fig. 4b), where a ~43 K TL peak lowering appears with increasing x . Note that the Tb_h (T_m) and Pr_h (T_m) in LiLuSiO_4 in Fig. 4a)-b) are about 35 K higher than that in Fig. 3b)-c). The compounds in Fig. 4 were synthesized ~2 years later with respect to that in Fig. 3b)-c), and the synthesis conditions may have been slightly different.

Fig. 4c) shows the TL glow curves for $\text{LiLu}_{1-x}\text{Y}_x\text{SiO}_4:0.01\text{Eu}^{3+},0.01\text{Bi}^{3+}$ after β irradiation. The TL glow peak Bi_h near 553 K gradually shifts ~35 K towards lower temperature when x increases. Note that the TL glow peak near 647 K named peak host_h , that will be attributed to hole liberation from intrinsic host-related hole trap(s), shifts only about 10 K towards lower temperature with increasing x . The derived energy level locations of the intrinsic defect(s) corresponding with these host_h TL peaks for $x = 0$ and $x = 1$ are shown in Fig. 1b). They are determined by adding the derived hole trap depths to the valence band top. Considering that hole liberation and transport

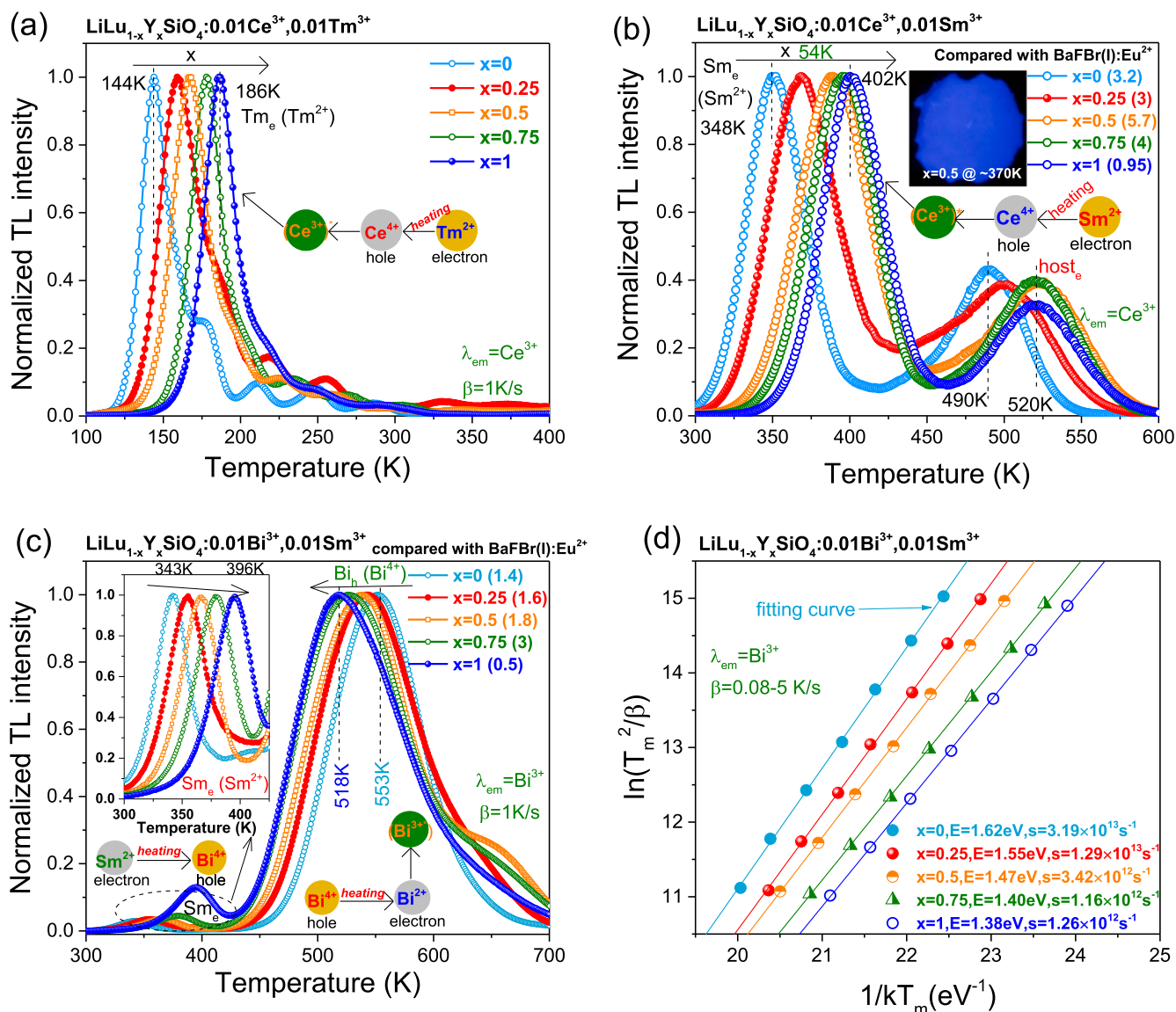


Fig. 5. TL glow curves for (a) $\text{LiLu}_{1-x}\text{Y}_x\text{SiO}_4:0.01\text{Ce}^{3+},0.01\text{Tm}^{3+}$, (b) $\text{LiLu}_{1-x}\text{Y}_x\text{SiO}_4:0.01\text{Ce}^{3+},0.01\text{Sm}^{3+}$, and (c) $\text{LiLu}_{1-x}\text{Y}_x\text{SiO}_4:0.01\text{Bi}^{3+},0.01\text{Sm}^{3+}$ recorded at a heating rate of 1 K/s after β irradiation. (d) Variable heating rate plots for Bi_h (Bi^{4+}) TL peaks of $\text{LiLu}_{1-x}\text{Y}_x\text{SiO}_4:0.01\text{Bi}^{3+},0.01\text{Sm}^{3+}$. The Ce^{3+} emission was monitored in a)-b), and the Bi^{3+} emission was selected in c)-d). A photograph for the $x = 0.5$ phosphor heated at ~370 K after Hg lamp charging is shown in b).

may be realized via V_k centre creation, the derived level locations of the intrinsic hole defect(s) may move up in the VRBE diagram in Fig. 1b).

3.3. Engineering electron liberation from Tm^{2+} and Sm^{2+} in $LiLu_{1-x}Y_xSiO_4$ solid solutions

In Fig. 1b) the conduction band bottom moves ~ 0.17 eV upward with the full substitution of Lu^{3+} by Y^{3+} in $LiLu_{1-x}Y_xSiO_4$ solid solutions, and an increase of the Ln^{3+} electron trapping depths is then expected. Fig. 5a) shows the low-temperature TL glow curves for $LiLu_{1-x}Y_xSiO_4:0.01Ce^{3+}, 0.01Tm^{3+}$ solid solutions after β irradiation. Here Ce^{3+} acts as a deep hole trap and Tm^{3+} as a less deep electron trap. With increasing x , the TL glow peak named peak Tm_e (Tm^{2+}) near 144 K shifts ~ 42 K towards higher temperature.

The Tm_e TL glow peak in $LiLu_{1-x}Y_xSiO_4$ in Fig. 5a) is at a too low temperature of 144–186 K for afterglow or storage phosphor applications. It needs to be shifted close to 400 K or even higher in order to avoid TL fading at RT for storage phosphor application. Fig. 1a) shows that Sm^{3+} acts as a ~ 0.47 eV deeper electron trap than Tm^{3+} . The storage phosphor properties of Sm^{3+} co-doped $LiLu_{1-x}Y_xSiO_4$ ($x = 0-1$) crystals were therefore explored.

Fig. 5b) and S11a) show the normalized and unnormalized TL glow curves for $LiLu_{1-x}Y_xSiO_4:0.01Ce^{3+}, 0.01Sm^{3+}$ solid solutions after β irradiation. With increasing x , the TL glow peak named peak Sm_e (Sm^{2+}), that will be assigned to electron liberation from Sm^{2+} , gradually shifts about 54 K from 348 K towards higher temperature in Fig. 5b). The shifting leads to almost 3 orders of magnitude decreased initial Ce^{3+} persistent luminescence in Fig. S11b), and less TL fading as shown in Fig. S11c). For the $x = 0.75$ phosphor after 100 min delay time, the integrated TL intensity between 300 and 723 K remains $\sim 85\%$, which is comparable to that of $BaFBr(I):Eu^{2+}$ (87%). The optimal concentration of the Sm^{3+} co-dopant at which Sm_e glow is most intense, is about 1% in $LiLu_{0.95}Y_{0.05}SiO_4:0.01Ce^{3+}, zSm^{3+}$ ($z = 0.1\%-1.6\%$) solid solutions as demonstrated in Fig. S12a). The legend of Fig. 5b) and S11a) provides the ratios of integrated TL between 300 and 723 K of $LiLu_{1-x}Y_xSiO_4:0.01Ce^{3+}, 0.01Sm^{3+}$ to that of the commercial X-ray storage phosphor $BaFBr(I):Eu^{2+}$ (Agfa-Gevaert). The maximal ratio of 5.7 is obtained when $x = 0.5$. Note that the TL peak near 490 K named peak $host_e$ for the $x = 0$ phosphor, that has been attributed to electron liberation from host intrinsic defect(s) in Refs. [53,54], first shifts ~ 30 K towards higher temperature from $x = 0$ to $x = 0.5$, but then remains constant near 520 K with further increasing x in $LiLu_{1-x}Y_xSiO_4:0.01Ce^{3+}, 0.01Sm^{3+}$.

Since Bi^{3+} can also act as a hole capturing centre, $LiLu_{1-x}Y_xSiO_4:0.01Bi^{3+}, 0.01Sm^{3+}$ was explored and its normalized TL glow curves after β irradiation are shown in Fig. 5c). The as recorded TL glow curves are shown in Fig. S15a). With increasing x , the Sm_e TL glow peak near 343 K shifts ~ 53 K towards higher temperature in the inset of Fig. 5c), which shares the same trend as that in $LiLu_{1-x}Y_xSiO_4:0.01Ce^{3+}, 0.01Sm^{3+}$ in Fig. 5b). The Bi_h TL glow peak near 553 K gradually shifts in the opposite direction ~ 35 K towards lower temperature when x increases. The same appears in $LiLu_{1-x}Y_xSiO_4:0.01Eu^{3+}, 0.01Bi^{3+}$ in Fig. 4c) above, where the recombination centre is Eu^{3+} instead of Bi^{3+} . The ratios of integrated TL between 300 and 723 K of $LiLu_{1-x}Y_xSiO_4:0.01Bi^{3+}, 0.01Sm^{3+}$ to that of

$BaFBr(I):Eu^{2+}$ are provided in the legend of Fig. 5c). The maximal ratio of 3 is observed when $x = 0.75$.

The hole trapping depths E (eV) of the Bi_h TL glow in $LiLu_{1-x}Y_xSiO_4:0.01Bi^{3+}, 0.01Sm^{3+}$ were derived using a variable heating rate plot and the first-order TL-recombination kinetics equation [11,57–59]:

$$\ln\left(\frac{T_m^2}{\beta}\right) = \frac{E}{kT_m} + \ln\left(\frac{E}{ks}\right) \quad (1)$$

in which k represents the Boltzmann constant (8.62×10^{-5} eV/K), s denotes the frequency factor (s^{-1}), and β is the heating rate of 0.08, 0.15, 0.3, 0.63, 1.25, 2.5, and 5 K/s. Fig. 5d) shows the variable heating rate plots for $LiLu_{1-x}Y_xSiO_4:0.01Bi^{3+}, 0.01Sm^{3+}$ that give the frequency factors as listed in column 2, and the trapping depths in column 4 of Table 1 for the Bi_h TL glow peak in Fig. 5c).

Considering that the doped content of Bi^{3+} is low, we assume that the above determined frequency factors also apply to $LiLu_{1-x}Y_xSiO_4:0.01Ce^{3+}, 0.01Ln^{3+}$ ($Ln = Sm$ or Tm), and $LiLu_{1-x}Y_xSiO_4:0.01Eu^{3+}, 0.01Ln^{3+}$ ($Ln = Tb$ or Pr). Assuming first-order TL-recombination kinetics, the hole trapping depths E (eV) for the Tb_h (Tb^{4+}) and Pr_h (Pr^{4+}) TL glow peaks in $LiLu_{1-x}Y_xSiO_4:0.01Eu^{3+}, 0.01Ln^{3+}$ in Fig. 4a)-b), the Tm_e (Tm^{2+}) TL peaks in $LiLu_{1-x}Y_xSiO_4:0.01Ce^{3+}, 0.01Tm^{3+}$ in Fig. 5a), and the Sm_e (Sm^{2+}) TL glow peaks in $LiLu_{1-x}Y_xSiO_4:0.01Ce^{3+}, 0.01Ln^{3+}$ in Fig. 5b) are determined by solving Eq. (1) with a temperature maximum (T_m) of a TL glow peak, $\beta = 1$ K/s, and the above-obtained s values as listed in column 2 of Table 1. The determined results are given in columns 6, 8, 10, and 12 of Table 1. Considering that there is a trap depth distribution in the prepared solid solutions, the obtained trap depths in Table 1 should be treated as indicative.

3.4. Engineering Bi^{4+} hole detrapping in $LiLu_{0.25}Y_{0.75}Si_{1-y}Ge_yO_4$ solid solutions

We explored further tailoring of the Bi_h (Bi^{4+}) TL glow peak in Bi^{3+} single doped $LiLu_{0.25}Y_{0.75}Si_{1-y}Ge_yO_4:0.01Bi^{3+}$ solid solutions. Fig. 1b) illustrates that the main effect of adding germanium is the $\sim 0.6-1.0$ eV lowering of the CB-bottom and in addition, the VB-top may change a few 0.1 eV. Fig. 6a) and S16 show the normalized and unnormalized TL glow curves for $LiLu_{0.25}Y_{0.75}Si_{1-y}Ge_yO_4:0.01Bi^{3+}$ solid solutions after β irradiation. The Bi_h TL glow peak near 538 K gradually shifts ~ 144 K towards 394 K from $y = 0$ to $y = 0.75$, implying that the VB-top moves up or the Bi^{3+} ground state moves down or both movements are combined. For the $y = 1$ phosphor, TL glow peaks near 327 K (weak), 371, 425, and 520 K emerge. Due to the lowering of the CB-bottom, we arrive at a situation where the Bi_e (Bi^{2+}) electron trap depth of $\sim 0.74 \pm 0.5$ eV becomes less deep than the Bi^{3+} hole trap depth of ~ 1.33 eV in $LiLuGeO_4$ in Fig. 1b). The same will apply to $LiLu_{0.25}Y_{0.75}GeO_4$. The dominant TL peak near 371 K is therefore tentatively attributed to electron release from Bi^{2+} to recombine with holes trapped at Bi^{4+} to give Bi^{3+} A-band emission as shown in Fig. S14h). The 371 K TL glow peak is referred to as the Bi_e (Bi^{2+}) glow peak. The TL peak shifting in Fig. 6a) results in more than a factor of 100 increased initial Bi^{3+} afterglow intensity in Fig. 6b), and stronger TL

Table 1

TL results for $LiLu_{1-x}Y_xSiO_4:0.01Bi^{3+}, 0.01Sm^{3+}$, $LiLu_{1-x}Y_xSiO_4:0.01Ce^{3+}, 0.01Ln^{3+}$ ($Ln = Sm$ or Tm), and $LiLu_{1-x}Y_xSiO_4:0.01Eu^{3+}, 0.01Ln^{3+}$ ($Ln = Tb$ or Pr) providing the frequency factors s (s^{-1}) and trap depths E (eV) for the Bi_h (Bi^{4+}), Tb_h (Tb^{4+}), Pr_h (Pr^{4+}), Sm_e (Sm^{2+}), and Tm_e (Tm^{2+}) TL glow peaks (T_m , K).

x	s	T_m Bi_h	E Bi_h	T_m Tb_h	E Tb_h	T_m Pr_h	E Pr_h	T_m Sm_e	E Sm_e	T_m Tm_e	E Tm_e
0	3.19×10^{13}	553	1.62	614	1.80	611	1.79	348	1.00	144	0.40
0.25	1.29×10^{13}	543	1.55	610	1.74	605	1.73	367	1.03	158	0.43
0.5	3.42×10^{12}	538	1.47	607	1.67	592	1.62	387	1.05	167	0.44
0.75	1.16×10^{12}	527	1.40	592	1.57	575	1.52	396	1.04	178	0.46
1	1.26×10^{12}	518	1.38	577	1.53	568	1.51	402	1.06	186	0.48

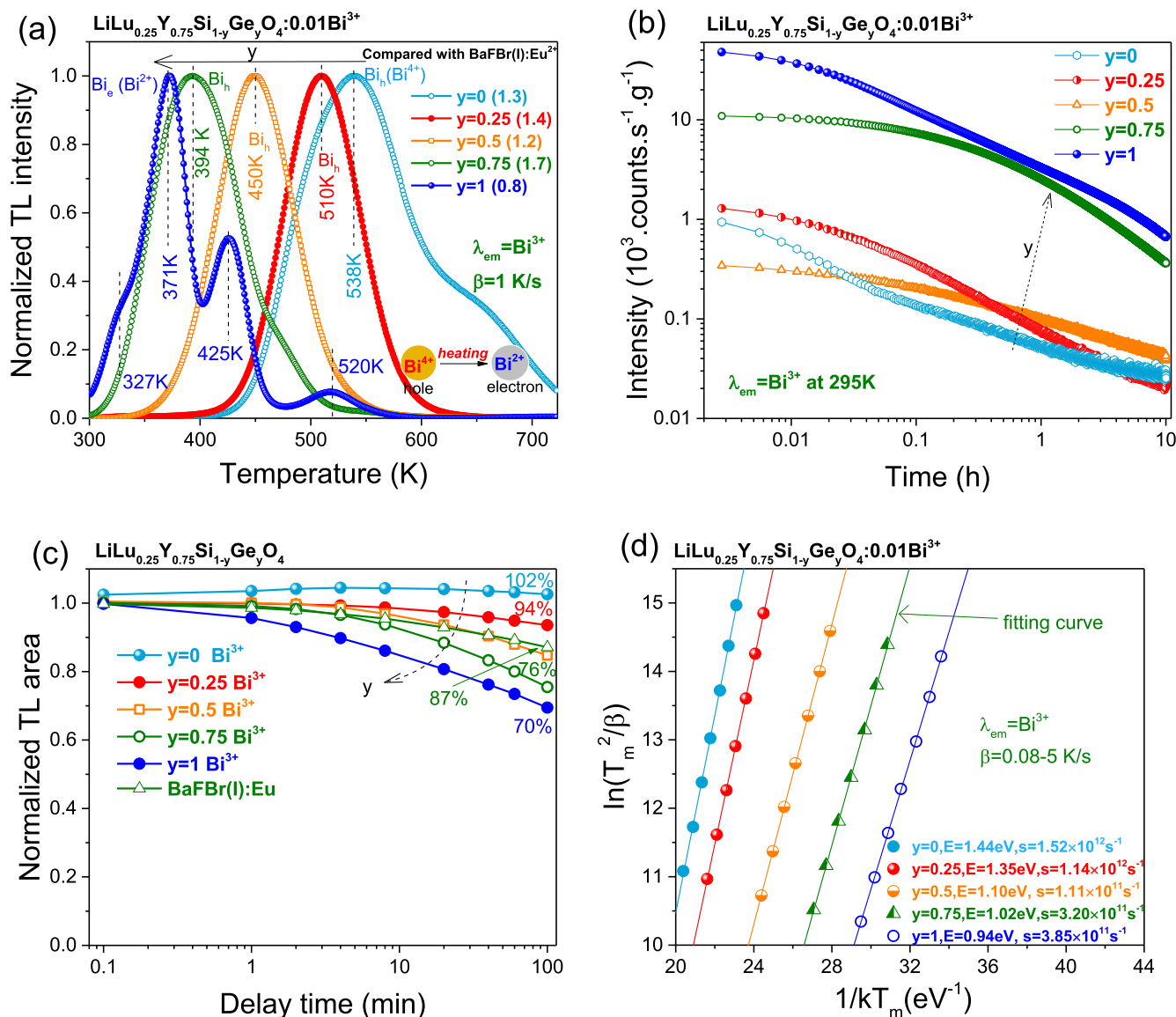


Fig. 6. (a) TL glow curves recorded at a heating rate of 1 K/s, (b) RT isothermal decay curves, (c) TL fading characteristics, and (d) variable heating rate plots for $\text{LiLu}_{0.25}\text{Y}_{0.75}\text{Si}_{1-y}\text{Ge}_y\text{O}_4:0.01\text{Bi}^{3+}$ solid solutions while monitoring the Bi^{3+} emission after β -ray irradiation.

fading as demonstrated in Fig. 6c). The ratios of integrated TL between 300 and 723 K of $\text{LiLu}_{0.25}\text{Y}_{0.75}\text{Si}_{1-y}\text{Ge}_y\text{O}_4:0.01\text{Bi}^{3+}$ to that of $\text{BaFBr}(\text{I}):\text{Eu}^{2+}$ are shown in the legend of Fig. 6a) and S16. The maximal ratio of 1.7 is obtained when $y = 0.75$.

The trapping depths E (eV) for the Bi_h (Bi^{4+}) and Bi_e (Bi^{2+}) TL glow peaks in $\text{LiLu}_{0.25}\text{Y}_{0.75}\text{Si}_{1-y}\text{Ge}_y\text{O}_4:0.01\text{Bi}^{3+}$ in Fig. 6a) were derived from variable heating rate plots using Eq. (1) where the heating rate changes between 0.08 and 5 K/s after β irradiation. Fig. 6d) shows the plots for $\text{LiLu}_{0.25}\text{Y}_{0.75}\text{Si}_{1-y}\text{Ge}_y\text{O}_4:0.01\text{Bi}^{3+}$ that gives the trapping depths and the frequency factors as listed in the legend of Fig. 6d).

Fig. 7a) and b) show the TL excitation (TLE) spectra for $\text{LiLu}_{0.25}\text{Y}_{0.75}\text{SiO}_4$ with $\text{Bi}^{3+}, \text{Sm}^{3+}$ and with Bi^{3+} only. For the $\text{LiLu}_{0.25}\text{Y}_{0.75}\text{Si}_{1-y}\text{Ge}_y\text{O}_4:0.01\text{Bi}^{3+}$ solid solution, the TLE spectrum is shown in Fig. 7c). Additional TLE spectra for other $\text{LiLu}_{0.25}\text{Y}_{0.75}\text{Si}_{1-y}\text{Ge}_y\text{O}_4:0.01\text{Bi}^{3+}$ phosphors can be found in Fig. S18. The Sm_2 TL glow peak near 410 K in Fig. 7a), and the Bi_h TL glow peak near 560 K in Fig. 7b) and near 530 K in Fig. 7c) can both be fitted using photons near 210 nm. Fig. 7d) shows the TL excitation (TLE) plots determined by integrating the TL glow peak between 450 and 723 K in Fig. 7b) and 300–723 K in Fig. 7c) and S18 for $\text{LiLu}_{0.25}\text{Y}_{0.75}\text{Si}_{1-y}\text{Ge}_y\text{O}_4:0.01\text{Bi}^{3+}$. Columns 2 and 3 of Table 2 compare

the TLE peak wavelengths with the photoluminescence excitation (PLE) peak wavelengths of Bi^{3+} D-bands for $\text{LiLu}_{0.25}\text{Y}_{0.75}\text{Si}_{1-y}\text{Ge}_y\text{O}_4:0.01\text{Bi}^{3+}$ from Fig. S19a). With increasing y , the TLE maximum near 210 nm gradually shifts 20 nm towards longer wavelength, which shares the same trend as that of the Bi^{3+} D-excitation band shifting in $\text{LiLu}_{0.25}\text{Y}_{0.75}\text{Si}_{1-y}\text{Ge}_y\text{O}_4:0.01\text{Bi}^{3+}$ phosphors.

3.5. Evaluating the potential application for information storage

The crystal synthesis of $\text{LiLu}_{0.25}\text{Y}_{0.75}\text{SiO}_4:0.01\text{Bi}^{3+}$ and $\text{LiLu}_{0.5}\text{Y}_{0.5}\text{SiO}_4:0.01\text{Ce}^{3+}, 0.005\text{Sm}^{3+}$ solid solutions was optimized in order to further increase the charge carrier storage capacity for achieving more efficient information storage. Fig. 8a) and 8c) show the TL glow curves and TL fading characteristics for the optimized samples. The ratio of integrated TL intensity between 300 and 800 K of $\text{LiLu}_{0.25}\text{Y}_{0.75}\text{SiO}_4:0.01\text{Bi}^{3+}$ to that of commercial $\text{Al}_2\text{O}_3:\text{C}$ or $\text{BaFBr}(\text{I}):\text{Eu}^{2+}$ is about 1.1 and 4.4. For $\text{LiLu}_{0.25}\text{Y}_{0.75}\text{SiO}_4:0.01\text{Bi}^{3+}$ after 10 h delay time, the integrated TL intensity remains 96%, which is ~20% higher than that of $\text{BaFBr}(\text{I}):\text{Eu}^{2+}$. The ratio of integrated TL intensity between 300 and 723 K of $\text{LiLu}_{0.5}\text{Y}_{0.5}\text{SiO}_4:0.01\text{Ce}^{3+}, 0.005\text{Sm}^{3+}$ to that of $\text{BaFBr}(\text{I}):\text{Eu}^{2+}$ is about 8.5, which is higher than that of ~4 in the

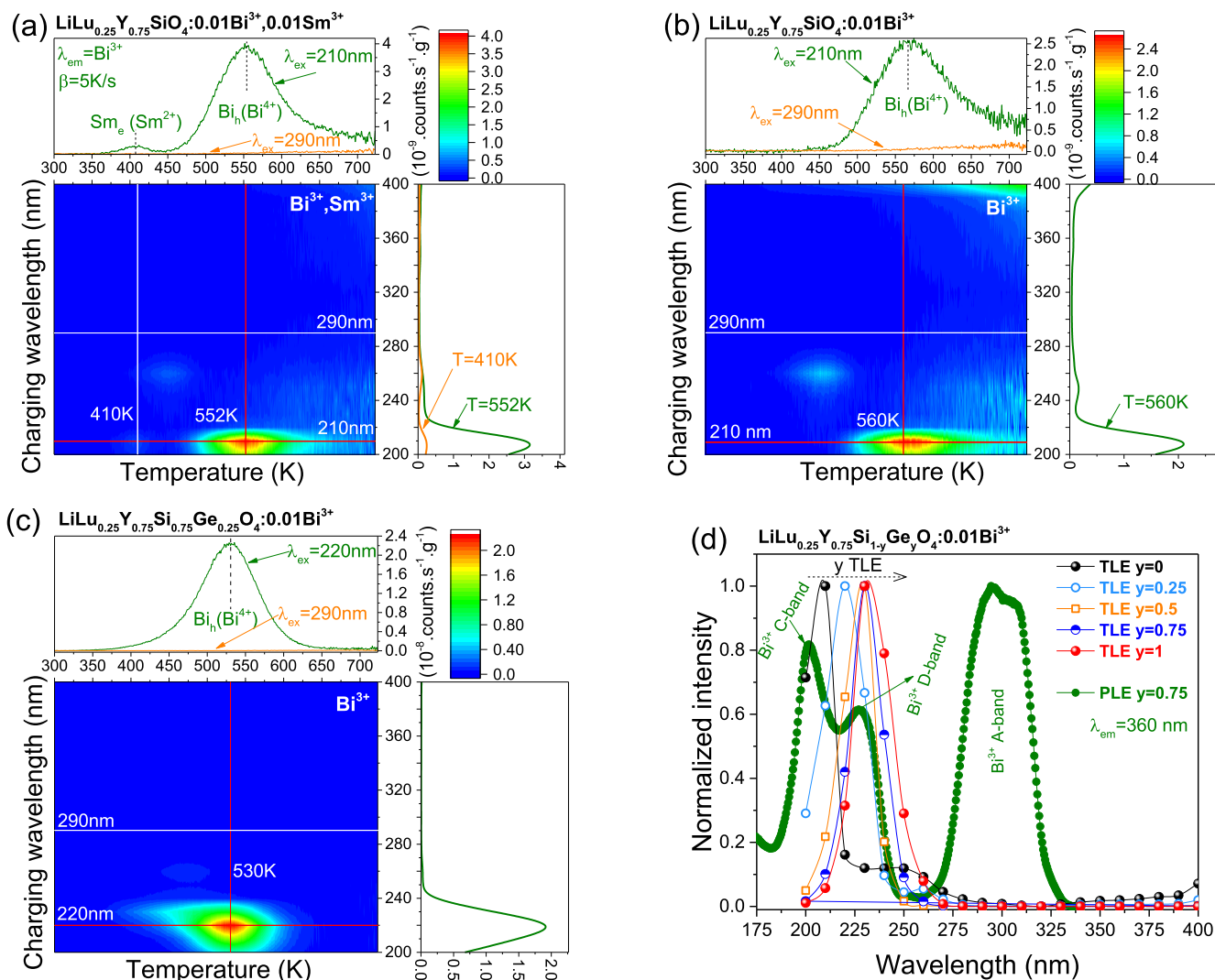


Fig. 7. (a)–(d) TL excitation (TLE) spectra recorded at a heating rate of 5 K/s for $\text{LiLu}_{0.25}\text{Y}_{0.75}\text{SiO}_4:0.01\text{Bi}^{3+}, 0.01\text{Sm}^{3+}$ and $\text{LiLu}_{0.25}\text{Y}_{0.75}\text{Si}_{1-y}\text{Ge}_y\text{O}_4:0.01\text{Bi}^{3+}$. The TLE plots in d) are constructed by integrating the TL glow peak between 450 and 723 K in b) and 300–723 K in c). The photoluminescence excitation spectrum monitoring the Bi^{3+} A-band emission (360 nm) for $\text{LiLu}_{0.25}\text{Y}_{0.75}\text{Si}_{1-y}\text{Ge}_y\text{O}_4:0.01\text{Bi}^{3+}$ ($y = 0.75$) at 10 K is shown in d).

Table 2

Comparison of the TL excitation (TLE) plots, the Bi_h and Bi_e TL glow peaks, and the Bi^{3+} D-excitation bands from spectroscopy for $\text{LiLu}_{0.25}\text{Y}_{0.75}\text{Si}_{1-y}\text{Ge}_y\text{O}_4:0.01\text{Bi}^{3+}$ ($y = 0-1$).

y	TLE peak	Bi^{3+} D-band	Bi_h TL peak at $\beta = 5 \text{ K/s}$	Bi_e TL peak at $\beta = 1 \text{ K/s}$
0	210 nm	207 nm	566 K	538 K
0.25	220 nm	214 nm	532 K	510 K
0.5	230 nm	223 nm	471 K	450 K
0.75	230 nm	227 nm	408 K	394 K
1	230 nm	230 nm	396 K (Bi_e)	371 K (Bi_e)

source Fig. 7d) Fig. S19a) Fig. 7b)-c) and S18 Fig. 6a)

optimized $\text{LiLuSiO}_4:\text{Ce}^{3+}, \text{Tm}^{3+}$ in Ref. [35] and of ~ 7 in the optimized $\text{NaYGeO}_4:0.01\text{Bi}^{3+}, 0.001\text{Eu}^{3+}$ in Ref. [55].

For storage phosphor application, the stored charge carriers during X-ray or other excitation source exposure are often read out by photon stimulation. Fig. 9 compares the TL glow curves of the optimized samples in this work after photon stimulation with various duration times. Additional TL curves for other $\text{LiLu}_{1-x}\text{Y}_x\text{Si}_{1-y}\text{Ge}_y\text{O}_4$ can be found in Fig. S24.

Fig. 9 and S24 demonstrate that 10 s of 475 nm photon stimulation releases $\sim 38, 54, 42, 95,$ and 41% of the charge carriers stored during β irradiation of $\text{LiLu}_{0.5}\text{Y}_{0.5}\text{SiO}_4:0.01\text{Ce}^{3+}, 0.01\text{Sm}^{3+}$, $\text{LiLu}_{0.25}\text{Y}_{0.75}\text{SiO}_4:0.01\text{Ce}^{3+}, 0.01\text{Sm}^{3+}$, $\text{LiLu}_{0.25}\text{Y}_{0.75}\text{SiO}_4:0.01\text{Bi}^{3+}$, $\text{BaFBr}(\text{I}):\text{Eu}^{2+}$, and $\text{Al}_2\text{O}_3:\text{C}$, respectively. The relative amount of released charge carriers in $\text{LiLu}_{0.5}\text{Y}_{0.5}\text{SiO}_4:0.01\text{Ce}^{3+}, 0.01\text{Sm}^{3+}$ in Fig. 9a) or $\text{LiLu}_{0.25}\text{Y}_{0.75}\text{SiO}_4:0.01\text{Bi}^{3+}$ in Fig. 9c) is smaller than that in $\text{BaFBr}(\text{I}):\text{Eu}^{2+}$, but their absolute amount is $\sim 2.4, 5.2$ times, and $\sim 1.3, 2.7$ times higher than that in $\text{BaFBr}(\text{I}):\text{Eu}^{2+}$ and $\text{Al}_2\text{O}_3:\text{C}$, respectively.

Fig. 9b)-c) shows that $\sim 94\%$ and $\sim 98\%$ of stored charge carriers can be liberated when the stimulation time increases to 1800 s. The same applies to other $\text{LiLu}_{0.25}\text{Y}_{0.75}\text{Si}_{1-y}\text{Ge}_y\text{O}_4$ phosphors as shown in Fig. S24g)-h). Fig. 9d) shows the stimulation spectra with different stimulation photon wavelength. For the $\text{LiLu}_{0.5}\text{Y}_{0.5}\text{SiO}_4:0.01\text{Ce}^{3+}, 0.01\text{Sm}^{3+}$ phosphor, a stimulation peak near 580 nm appears. The information stored by the $\text{LiLu}_{0.25}\text{Y}_{0.75}\text{SiO}_4:0.01\text{Bi}^{3+}$ phosphor is erased more efficiently at 410 nm.

Fig. 10 demonstrates proof-of-concept information storage and readout using the developed phosphor. $\text{LiLu}_{0.5}\text{Y}_{0.5}\text{SiO}_4:0.01\text{Ce}^{3+}, 0.01\text{Sm}^{3+}$ phosphor is first dispersed in a ~ 2 mm thick silicone gel to form “plate I”, which is then placed underneath a chicken bone to be X-ray exposed as demonstrated in Fig. 10a2). “Plate I” was heated to ~ 370 K and after 12 and 32s a photo

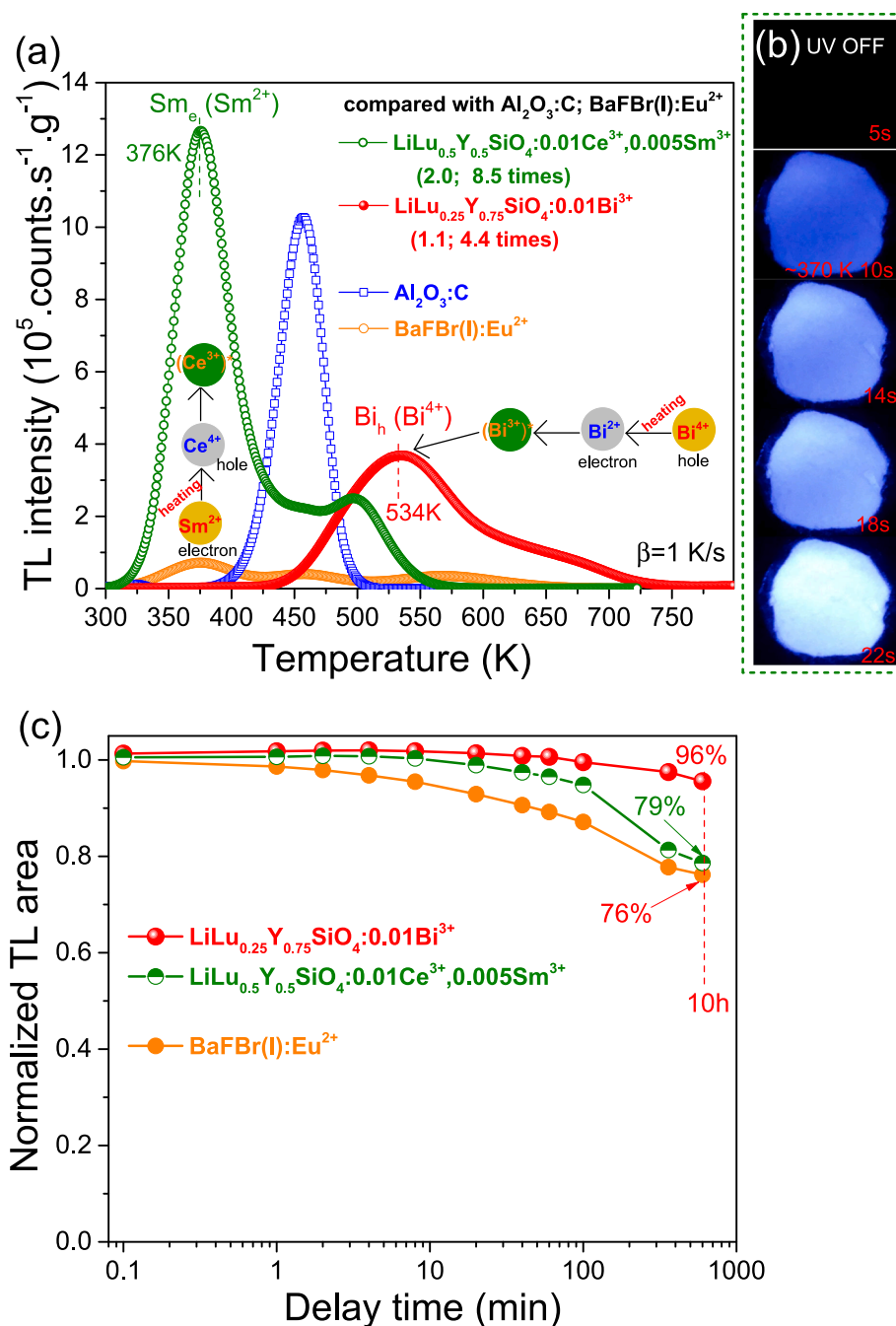


Fig. 8. (a) TL glow curves at $\beta = 1$ K/s, and (c) TL fading characteristics for the optimized $\text{LiLu}_{0.25}\text{Y}_{0.75}\text{SiO}_4:0.01\text{Bi}^{3+}$ and $\text{LiLu}_{0.5}\text{Y}_{0.5}\text{SiO}_4:0.01\text{Ce}^{3+}, 0.005\text{Sm}^{3+}$ after β -ray irradiation. (b) Photographs of thermally stimulated emission of $\text{LiLu}_{0.5}\text{Y}_{0.5}\text{SiO}_4:0.01\text{Ce}^{3+}, 0.005\text{Sm}^{3+}$ at ~ 370 K with different duration time after Hg lamp charging.

of the afterglow was made. The X-ray image of the chicken bone shape appears as a weaker thermally stimulated Ce^{3+} emission intensity in Fig. 10a3) and a4). This is due to the absorption of X-rays by the chicken bone during X-ray exposure. The resolution of the image in Fig. 10a3) and a4) is rather poor, but when an image was made with a ~ 0.5 mm thick plate II it improves as shown in Fig. 10a6). The similar applies to another X-ray image of a chicken bone stored in “plate III” in Fig. S31a4)–a6), where the $\text{LiLu}_{0.25}\text{Y}_{0.75}\text{SiO}_4: 0.01\text{Bi}^{3+}, 0.01\text{Sm}^{3+}$ storage phosphor was used. Here the X-ray image is obtained because of afterglow from hole liberation from Bi^{4+} and recombination with Bi^{2+} followed by energy transfer from Bi^{3+} to Sm^{3+} , as illustrated in Fig. S31a7). Note that the used optical sensor of the smartphone is not sensitive to the main thermally stimulated Bi^{3+} emission near 360 nm

in $\text{LiLu}_{0.25}\text{Y}_{0.75}\text{SiO}_4:0.01\text{Bi}^{3+}, 0.01\text{Sm}^{3+}$.

“Plate I” in Fig. 10b1) is placed underneath a black mask as shown in Fig. 10b2). $\text{LiLu}_{1-x}\text{Y}_x\text{SiO}_4:0.01\text{Ce}^{3+}, 0.01\text{Sm}^{3+}$ can be charged by 260 nm light as shown in Fig. S13. When the UV-light near 260 nm passes through the open area of the black mask it charges “plate I”. The information of text of “LMG TUD TSL Ce^{3+} ” is then stored in the “plate I” in Fig. 10b3). The text is not visible in the dark when the UV-light is switched off in Fig. 10b4). The text emerges again in Fig. 10b5) when the “plate I” is heated to ~ 370 K with duration time of ~ 15 s because of thermally stimulated Ce^{3+} emission. The mechanism is demonstrated in Fig. 10b6).

A QR code printed on a sheet of white paper in Fig. 10c1) was generated by the text of “This is a nice storage phosphor for information

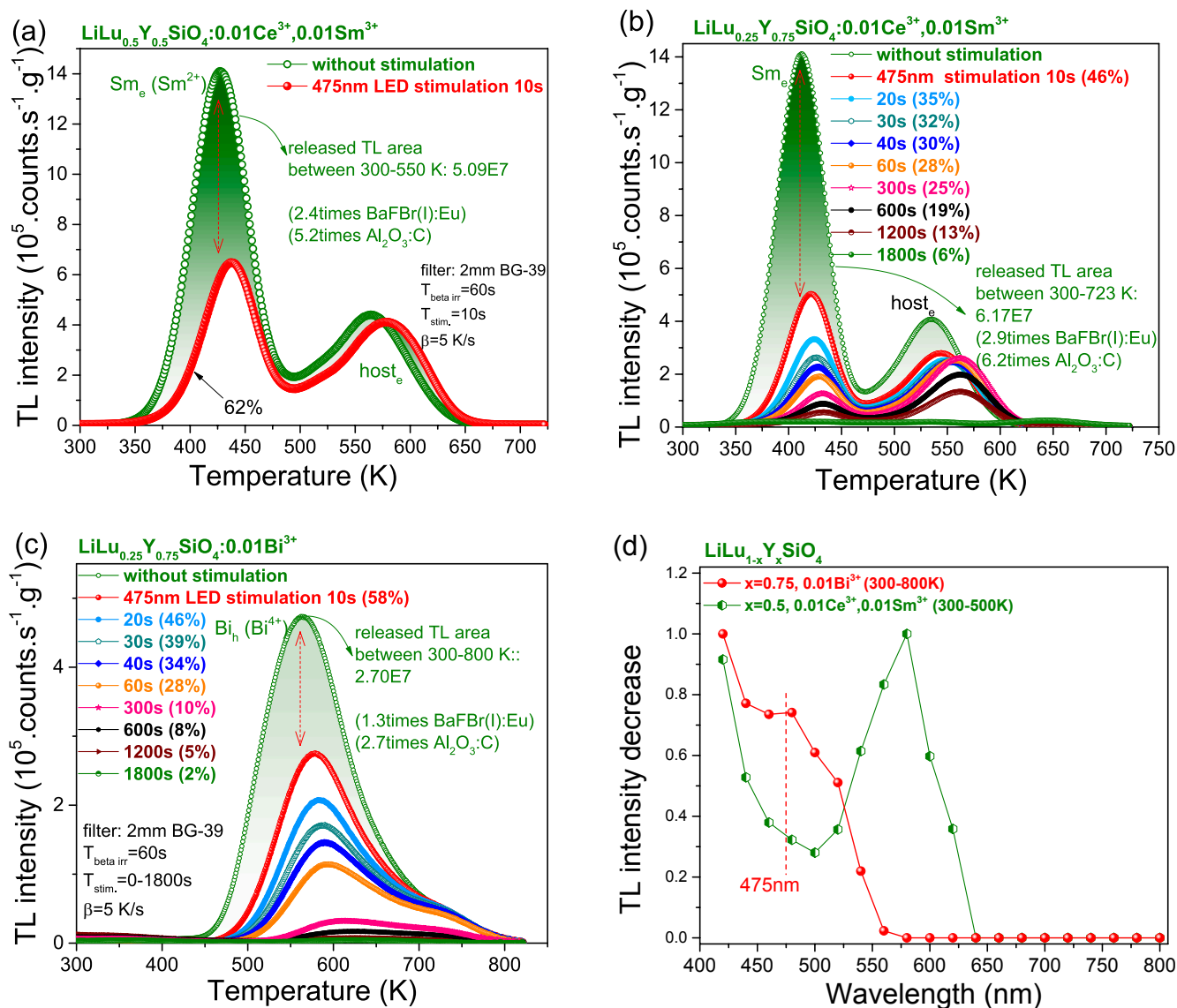


Fig. 9. TL glow curves at $\beta = 5 \text{ K/s}$ for (a) $\text{LiLu}_{0.5}\text{Y}_{0.5}\text{SiO}_4:0.01\text{Ce}^{3+},0.01\text{Sm}^{3+}$, (b) $\text{LiLu}_{0.25}\text{Y}_{0.75}\text{SiO}_4:0.01\text{Ce}^{3+},0.01\text{Sm}^{3+}$, and (c) $\text{LiLu}_{0.25}\text{Y}_{0.75}\text{SiO}_4:0.01\text{Bi}^{3+}$ recorded after β -ray irradiation and after β -ray irradiation followed by 475 nm LED optical stimulation with different duration time. (d) Stimulation spectra where the decrease of integrated TL intensity between 300 and 500 K for $\text{LiLu}_{0.5}\text{Y}_{0.5}\text{SiO}_4:0.01\text{Ce}^{3+},0.01\text{Sm}^{3+}$ in a) and between 300 and 800 K for $\text{LiLu}_{0.25}\text{Y}_{0.75}\text{SiO}_4:0.01\text{Bi}^{3+}$ in c) after different energy photon stimulation.

storage from TUD!" with computer software. The QR code is visible in the dark in Fig. 10c2) because of the $\sim 370 \text{ K}$ thermally stimulated Ce^{3+} emission from "plate I" underneath the paper as a backlight display source shining through the sheet in Fig. 10c2). The QR code was scanned using a mobile phone software in the dark to read out the hidden text above as demonstrated in Fig. 10c3).

4. Discussion

Based on low-temperature (10 K) photoluminescence spectroscopy in Ref. [55], the constructed vacuum referred binding energy (VRBE) diagrams including bismuth and lanthanide levels for LiLuSiO_4 related family of compounds are shown in Fig. 1 and S1. We will show how these VRBE schemes can be verified and made more accurate by thermoluminescence study, and how they guide the design of both the electron and hole trapping processes in the lanthanide and/or bismuth doped $\text{LiRE}(\text{Si},\text{Ge})\text{O}_4$ ($\text{RE} = \text{Y}$ or Lu) towards storage phosphors with high charge carrier storage capacity for information storage. Here let us call this approach the 'engineering game'.

The essence of the game is to combine a hole trapping defect with an electron trapping defect in a controlled fashion. In sequence of decreasing hole trap depths in Fig. 1a) and b) one may select Ce^{3+} , $\text{Pr}^{3+} \sim \text{Tb}^{3+}$, and Bi^{3+} where Ce^{3+} is the deepest h-trap and Bi^{3+} is the shallowest h-trap. In sequence of decreasing electron trap depths one may select Eu^{3+} , Bi^{3+} , Yb^{3+} , Sm^{3+} , and Tm^{3+} . We will call these trapping centres 'the players'. In addition to these controlled trapping centres one has to deal with the intrinsic e-traps and h-traps, and in this work we will show how one may discriminate one type from another.

Fig. 1b) illustrates that our 'playing field' are the solid solutions $\text{LiLu}_{1-x}\text{Y}_x\text{Si}_{1-y}\text{Ge}_y\text{O}_4$ where we have focused on the silicates ($y = 0$). A small excursion was made for $x = 0.75$ where y was changed from 0 to 1.

The 'rules of the game' are actually the physical mechanism of carrier trapping and recombination. 1) If the hole trap is deeper than the electron trap, then the electron is released at a lower temperature than the hole. Recombination takes place at the hole centre leading to hole-trap luminescence. 2) If the e-trap is deeper than the h-trap, the hole will be released at a lower temperature to recombine with the electrons

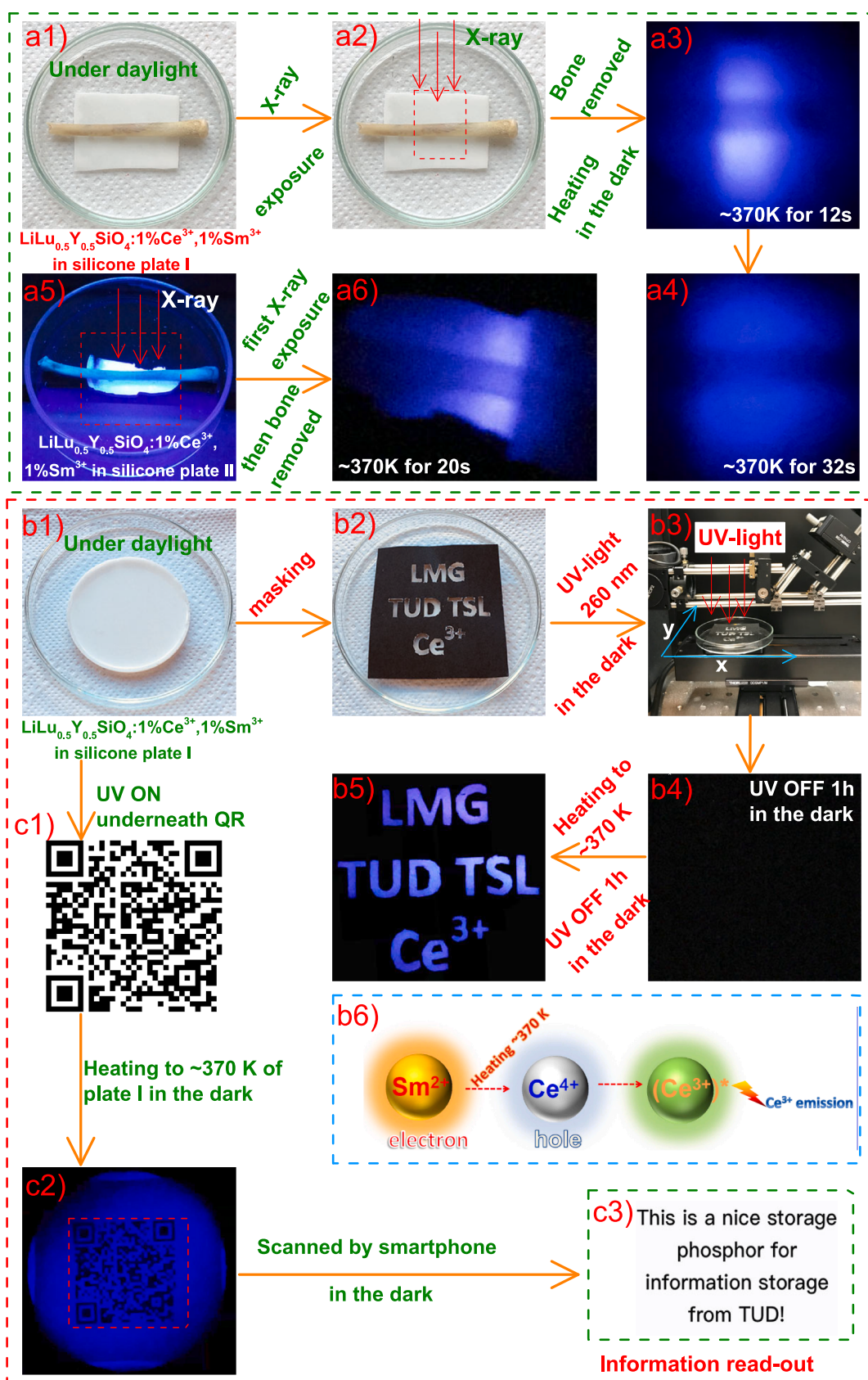


Fig. 10. Proof-of-concept information storage application by using $\text{LiLu}_{0.5}\text{Y}_{0.5}\text{SiO}_4:0.01\text{Ce}^{3+},0.01\text{Sm}^{3+}$ dispersed in the silicone gel plates I and II. Information storage and display of an X-ray photograph of a chicken bone in a1)–a6), of text of LMG TUD TSL Ce^{3+} in b1)–b5), and of a QR code on a paper in the dark in c1)–c3). b6) illustrates the thermally stimulated luminescence process for b5). The chicken bone was removed before heating in a3)–a4), and a6), and the mask was not removed during heating in b5). The thickness is $\sim 2\text{ mm}$ for plate I in a2) and $\sim 0.5\text{ mm}$ for plate II in a5). Both the plates in a2) and a5) were heated to $\sim 370\text{ K}$ for 3 min to empty all traps in the dark before X-ray exposure.

at the e-trap leading to e-trap emission. 3) by changing the VRBE at the VB-top via changing x or y in solid solutions the hole trapping depths will change likewise. 4) changing the VRBE at the CB-bottom by changing x or y in solid solutions affects the e-trapping depths.

The 'strategy of the game' is to find combinations of e-trap and h-trap for a specific purpose and then engineer x and y towards either optimal storage phosphor or optimal afterglow phosphor performance.

4.1. Playing with the colour of recombination emission

Guided by the VRBE diagram in Fig. 1a), the combination of a deep h-trap formed by Ln^{3+} ($\text{Ln} = \text{Ce}, \text{Tb}, \text{or Pr}$) or Bi^{3+} with a less deep e-trap formed by Tm^{3+} or Sm^{3+} was explored with the aim to engineer the recombination emission in $\text{LiLu}_{1-x}\text{Y}_x\text{SiO}_4$. Compared with the Ce^{3+} or Bi^{3+} single doped LiLuSiO_4 in Fig. S7a), an additional TL glow peak near 144 K emerges in Tm^{3+} -codoped LiLuSiO_4 in Fig. 5a) and S7a). The corresponding 0.40 eV electron trap depth in Table 1 is smaller than the predicted hole trap depths of Ce^{3+} , Tb^{3+} , Pr^{3+} , and Bi^{3+} . Considering the largely systematic error margins of few 0.1 eV in VRBE diagrams based on broad charge transfer band transitions [13,60], the 0.40 eV is still regarded as consistent with the ~ 0.62 eV electron trap depth of Tm^{3+} in the VRBE diagram in Fig. 1a). The 144 K Tm_e TL glow peak is therefore attributed to electron liberation from Tm^{2+} to recombine with holes at Ce^{4+} , Pr^{4+} , Tb^{4+} , and Bi^{4+} to give characteristic 5d-4f or 4f-4f emission of Ce^{3+} , Pr^{3+} , and Tb^{3+} , and Bi^{3+} A-band emission in Fig. S7a). This is further supported in Fig. S7b) where a same Tm_e TL peak near 186 K appears in all four Tm^{3+} -codoped $\text{LiY-SiO}_4:0.01\text{Ln}^{3+}, 0.01\text{Tm}^{3+}$ ($\text{Ln} = \text{Ce}, \text{Pr}, \text{or Tb}$) and $\text{LiY-SiO}_4:0.01\text{Bi}^{3+}, 0.01\text{Tm}^{3+}$ samples. These results imply that one may engineer the recombination emission by the choice of deep hole trapping centres of Ce^{3+} , Pr^{3+} , Tb^{3+} , or Bi^{3+} when combined with the less deep Tm^{3+} electron trapping centre.

Fig. 1a) illustrates that one may also engineer the recombination colour by combining the deep e-traps of Eu^{3+} and Bi^{3+} with less deep h-traps of Tb^{3+} , Pr^{3+} , and Bi^{3+} in LiLuSiO_4 . Indeed hole liberation from Tb^{4+} , Pr^{4+} , and Bi^{4+} that recombines with electrons at Eu^{2+} to give characteristic Eu^{3+} 4f-4f emission was identified, which is evidenced by the TL emission spectra and the corresponding TL glow peaks Tb_h , Pr_h , and Bi_h in Fig. 3b)-d). If the e-trap of Eu^{3+} is not present as in Fig. 3e) and 3f), the Bi_h TL glow peaks near 532 K and near 510 K with Bi^{3+} A-band emission appear because of the hole liberation from Bi^{4+} to recombine with electrons captured at Bi^{2+} . Here it demonstrates that one can tailor the recombination emission from Eu^{3+} 4f-4f emission to Bi^{3+} A-band emission by replacing the e-trap of Eu^{3+} by that of Bi^{3+} and using the hole liberation from Bi^{4+} .

4.2. Playing with the electron trapping depth

Fig. 1a) and 1b) predict that Sm^{3+} acts as a ~ 0.46 eV deeper electron trap than Tm^{3+} which would correspond to a higher T_m for the corresponding TL glow peak. Fig. S7c) shows that indeed an additional TL peak near 345 K emerges in all the three Sm^{3+} -codoped $\text{LiLuSiO}_4:0.01\text{Ln}^{3+}, 0.01\text{Sm}^{3+}$ ($\text{Ln} = \text{Pr}, \text{Tb}, \text{or Ce}$) compared with the Ln^{3+} single doped samples. The ~ 345 K TL peak also appears in $\text{LiLuSiO}_4:0.01\text{Bi}^{3+}, 0.01\text{Sm}^{3+}$ in Fig. 5c). The experimentally derived 1.0 eV electron trap depth for the 345 K TL peak in Table 1 is consistent with the predicted ~ 1.08 eV electron trap depth of Sm^{3+} and is less deep than the predicted hole trap depths of Pr^{3+} , Tb^{3+} , Ce^{3+} , and Bi^{3+} based on the VRBE scheme in Fig. 1a). We therefore attribute the TL peak near 345 K to the electron release from Sm^{2+} to recombine with holes at Pr^{4+} , Tb^{4+} , Ce^{4+} , and Bi^{4+} generating characteristic Pr^{3+} , Tb^{3+} , Ce^{3+} , and Bi^{3+} emission, respectively. The above result implies that one may engineer the electron trap depth by the choice of lanthanides like Tm^{3+} and Sm^{3+} . Since the TL peak shifts about 200 K close to room temperature by replacing the e-trap of Tm^{3+} by that of Sm^{3+} in the $\text{LiLuSiO}_4:0.01\text{Ce}^{3+}, 0.01\text{Ln}^{3+}$ in Fig. 5a)-b), Ce^{3+}

afterglow emerges in $\text{LiLuSiO}_4:0.01\text{Ce}^{3+}, 0.01\text{Sm}^{3+}$ in Fig. S11b). One may again engineer the afterglow colour by replacing the hole trapping centre of Ce^{3+} by Tb^{3+} or Pr^{3+} , producing typical Tb^{3+} and Pr^{3+} afterglow as demonstrated in Fig. S10.

Above the players were Tm and Sm but one may also enlarge the playing field by studying solid solutions. The results for Ln^{3+} and/or Bi^{3+} doped $\text{LiLu}_{1-x}\text{Y}_x\text{SiO}_4$ solid solutions in Fig. 5a)-c) demonstrate the electron trap depth tailoring of Tm^{3+} and Sm^{3+} by conduction band engineering. Here Ce^{3+} and Bi^{3+} act as deep hole capturing centres and Tm^{3+} and Sm^{3+} are less deep electron trapping centres. An about 0.1 eV trap depth increase is determined from both the Sm_e and Tm_e TL glow peaks in columns 10 and 12 of Table 1 when x increases from 0 to 1. It indicates that the conduction band bottom moves up by ~ 0.1 eV in $\text{LiLu}_{1-x}\text{Y}_x\text{SiO}_4$ with increasing x, which is to be compared with the predicted 0.17 eV increase in the stacked VRBE scheme as shown in Fig. 1b). We therefore attribute the about 50 K shifting of Tm_e and Sm_e TL peaks towards higher temperature to the increased activation energy for electron liberation from Tm^{2+} and Sm^{2+} as a result of conduction band rising with increasing x in $\text{LiLu}_{1-x}\text{Y}_x\text{SiO}_4$. The above result also demonstrates that thermoluminescence is a sensitive technique to determine a small (~ 0.1 eV) energy difference in a VRBE scheme.

The above results imply that one may design a storage phosphor via tailoring the electron trap depth by a combination of conduction band engineering and a choice of Ln^{3+} like the above Tm^{3+} and Sm^{3+} codopants. By further synthesis optimization, a good storage phosphor may appear like $\text{LiLu}_{0.5}\text{Y}_{0.5}\text{SiO}_4:0.01\text{Ce}^{3+}, 0.005\text{Sm}^{3+}$ in Fig. 8a)-b) where after β irradiation its integrated TL intensity between 300 and 723 K is about 2 and 8.5 times higher than that of commercial $\text{Al}_2\text{O}_3:\text{C}$ and $\text{BaFBr}(\text{I}):\text{Eu}^{2+}$ storage phosphors.

Intrinsic host-related electron traps can also be very important for a high charge carrier storage capacity [35]. Using Eq. (1) with the frequency factor in column 2 of Table 1 and $\beta = 1$ K/s, the trapping depths for the host_e TL peaks in $\text{LiLu}_{1-x}\text{Y}_x\text{SiO}_4:0.01\text{Ce}^{3+}, 0.01\text{Sm}^{3+}$ in Fig. 5b) are determined between ~ 1.43 and ~ 1.38 eV. They are ~ 3 eV less deep than the predicted Ce^{3+} hole trap depth in Fig. 1a). We therefore attribute these TL peaks to host-related intrinsic electron traps. The VRBE at the intrinsic defect(s) corresponding with these TL peaks is indicated in Fig. 1b). It is derived by subtracting the experimentally determined electron trap depth from the conduction band bottom. The VRBE in LiYSiO_4 is different from that in LiLuSiO_4 indicating that the VRBE at the intrinsic defect(s) is more dependent on the compound composition than that of Sm^{2+} in $\text{LiLu}_{1-x}\text{Y}_x\text{SiO}_4:0.01\text{Ce}^{3+}, 0.01\text{Sm}^{3+}$.

4.3. Playing with the hole trapping depth

The vacuum referred binding energy (VRBE) scheme for LiLuSiO_4 in Fig. 1a) illustrates that Ce^{3+} , Pr^{3+} , Tb^{3+} , and Bi^{3+} will act as ~ 3.89 , ~ 2.04 , ~ 2.22 , and ~ 1.90 eV deep hole trapping centres, while Eu^{3+} , Yb^{3+} , and Bi^{3+} will act as ~ 2.34 , ~ 1.90 , and $\sim 1.81 \pm 0.5$ eV deep electron trapping centres in LiLuSiO_4 . Holes captured to form Pr^{4+} , Tb^{4+} , and Bi^{4+} are then predicted to be released earlier, i.e., at a lower temperature, than the electrons at Eu^{2+} to upon recombination produce characteristic red 4f-4f emission of Eu^{3+} .

Using Eq. (1) with the frequency factor in column 2 of Table 1 and $\beta = 1$ K/s, the trapping depths for TL peaks denoted I_h to V_h in LiLuSiO_4 in Fig. 3a) are determined to be ~ 1.08 , 1.22, 1.45, 1.63, and 2.21 eV, which are less deep than the predicted Eu^{3+} electron trap depth of ~ 2.34 eV in Fig. 1a). These I_h - V_h TL peaks are therefore attributed to host-related intrinsic hole traps. We have drawn the derived level location for the I_h hole trap in Fig. 1b). The trapping depths for TL peaks Tb_h near 572 K and Pr_h near 582 K in Fig. 3b)-c) are derived to be ~ 1.67 , and ~ 1.70 eV, respectively. During TL-readout, the activation energies required to liberate holes from Tb^{4+} (1.67 eV) and from Pr^{4+} (1.70 eV) are about 0.7 eV smaller than that to liberate electrons from Eu^{2+} (~ 2.34 eV). Therefore, the holes liberate from Tb^{4+} and Pr^{4+} to

recombine with the electrons captured at Eu^{2+} to generate the TL glow peaks Tb_h and Pr_h with characteristic red 4f-4f emission of Eu^{3+} .

Columns 6 and 8 of Table 1 show that the experimentally determined average hole trap depth for both Tb^{3+} and Pr^{3+} is ~ 1.80 eV in LiLuSiO_4 , and ~ 1.52 eV in LiYSiO_4 , respectively. It is about 0.33, and 0.61 eV smaller compared with the ones estimated from the VRBE scheme (2.22 eV for Tb^{3+} and 2.04 eV for Pr^{3+}) in Fig. 1a). Similar deviation about 0.6 eV appeared in YPO_4 [13], and about 0.3 eV emerged in GdAlO_3 [2]. It may suggest there are errors and uncertainties in VRBE scheme construction. However, holes generated in the valence band tend to create a V_k centre by bonding with two neighbouring oxygen anions [61–63]. Bonding means that the hole state moves up in a VRBE diagram [2,13,64]. The ~ 0.33 , and ~ 0.61 eV energy differences in LiLuSiO_4 and LiYSiO_4 could also be largely attributed to the binding energies of the V_k centres. Upon thermal stimulation during TL-readout, holes are liberated from Tb^{4+} or Pr^{4+} to form a V_k centre, which then migrates to recombine with electrons trapped at Eu^{2+} to generate characteristic 4f-4f emission of Eu^{3+} in LiLuSiO_4 or LiYSiO_4 .

The VRBE scheme in Fig. 1a) was constructed with the method outlined in Ref. [60] where the ground state of Pr^{3+} is 0.18 eV below that of Tb^{3+} . One then expects that the Pr_h TL glow peak appears at about 60–70 K lower temperature than the Tb_h TL glow peak. In Refs. [65,66] experimental evidence was presented that the ground state of Pr^{3+} and Tb^{3+} should be at similar energy and also slightly compound dependent. This is now further confirmed in this work. The Pr^{4+} TL glow peak appears at only about 10 K lower temperature than that of Tb^{4+} in $\text{LiLu}_{1-x}\text{Y}_x\text{SiO}_4:0.01\text{Eu}^{3+},0.01\text{Ln}^{3+}$ ($\text{Ln} = \text{Tb}$ or Pr) in Fig. 4a)-b) and $\text{YPO}_4:0.01\text{Eu}^{3+},0.01\text{Ln}^{3+}$ in Ref. [13]. Columns 6 and 8 of Table 1 show that the experimentally derived hole trap depth of Tb^{3+} is almost the same as that of Pr^{3+} in $\text{LiLu}_{1-x}\text{Y}_x\text{SiO}_4$.

Fig. 1a) illustrates that Bi^{3+} acts as a ~ 1.90 eV deep hole trap, while Eu^{3+} and Bi^{3+} act as ~ 2.34 and $\sim 1.81 \pm 0.5$ eV deep electron traps in LiLuSiO_4 . The TLEM plots in Fig. 3d)-e) for $\text{LiLu}_{0.5}\text{Y}_{0.5}\text{SiO}_4:0.01\text{Eu}^{3+},0.01\text{Bi}^{3+}$ and $\text{LiLu}_{0.5}\text{Y}_{0.5}\text{SiO}_4:0.01\text{Bi}^{3+},0.01\text{Sm}^{3+}$ share the same Bi_h TL peak near 532–535 K. A slightly higher Bi_h TL peak near 553 K emerges in LiLuSiO_4 in Fig. 4c). Bi_h hole trap depth in LiLuSiO_4 is determined to be 1.62 eV in Table 1, which is ~ 0.3 eV smaller than that predicted by the Bi^{3+} $^1\text{S}_0$ ground state level based on Bi^{3+} D-band in the VRBE diagram in Fig. 1a). Like the Tb^{4+} and Pr^{4+} hole detrapping processes discussed above, the ~ 0.3 eV energy difference may be due to the errors and uncertainties in VRBE diagram construction, but also could be largely attributed to the binding energy of the V_k centre. Note that the Bi^{3+} hole trap depth (1.90 eV) is less deep than the predicted electron trap depth of Eu^{3+} (~ 2.34 eV) in Fig. 1a). During TL-readout, a hole is therefore released from Bi^{4+} earlier to generate a V_k centre, which then migrates to recombine with electrons at Eu^{2+} to produce the Bi_h TL peak near 535 K with Eu^{3+} 4f-4f emission in $\text{LiLu}_{0.5}\text{Y}_{0.5}\text{SiO}_4$ in Fig. 3d). Considering that the same Bi_h TL peak appears in Fig. 3e) where Bi^{3+} is the recombination centre instead of Eu^{3+} , hole liberation from Bi^{4+} to recombine with electrons at Bi^{2+} to produce Bi^{3+} A-band emission is supported. The above result also supports the assumption that the VRBE at the Bi^{2+} ground state in LiRESiO_4 is near about -3.5 ± 0.5 eV, and that Bi^{3+} acts as a deeper electron trap than hole trap. The Sm^{3+} 4f-4f emission in Fig. 3e) is then attributed to energy transfer of $\text{Bi}^{3+} \rightarrow \text{Sm}^{3+}$.

The TL results for Ln^{3+} and/or Bi^{3+} doped $\text{LiLu}_{1-x}\text{Y}_x\text{SiO}_4$ in Figs. 4 and 5c), and $\text{LiLu}_{0.25}\text{Y}_{0.75}\text{Si}_{1-y}\text{Ge}_y\text{O}_4:0.01\text{Bi}^{3+}$ solid solutions in Fig. 6a) demonstrate the hole trap depth tailoring of Tb_h , Pr_h , and Bi_h TL peaks. An about 0.25 eV trap depth decrease is derived from the Bi_h , Tb_h , and Pr_h TL peaks in columns 4, 6, and 8 of Table 1 with increasing x in $\text{LiLu}_{1-x}\text{Y}_x\text{SiO}_4$. It is to be compared with the ~ 0.1 eV raising of the VB-top in the stacked VRBE diagram in Fig. 1b). We therefore attribute the about 40 K shifting of Tb_h , Pr_h , and Bi_h TL peaks towards lower temperature in Fig. 4a)-c) to the decreased activation energy for hole

release from Tb^{4+} , Pr^{4+} , and Bi^{4+} because of valence band rising with increasing x in $\text{LiLu}_{1-x}\text{Y}_x\text{SiO}_4$. This again demonstrates that a small (~ 0.1 eV) energy difference in a VRBE diagram can be probed using the sensitive thermoluminescence technique.

Fig. 6a) and column 5 of Table 2 show that the Bi_h (Bi^{4+}) TL peak can be lowered from ~ 538 K to ~ 394 K by increasing y from 0 to 0.75 in $\text{LiLu}_{0.25}\text{Y}_{0.75}\text{Si}_{1-y}\text{Ge}_y\text{O}_4:0.01\text{Bi}^{3+}$. It corresponds with ~ 0.42 eV decrease of the Bi^{3+} hole trap depths as determined from the variable heating rate plots in Fig. 6d). This is to be compared with the predicted ~ 0.57 eV decrease of the Bi^{3+} hole trap depth when Si^{4+} is totally replaced for Ge^{4+} in $\text{LiLuSi}_{1-y}\text{Ge}_y\text{O}_4$ in the stacked VRBE diagram in Fig. 1b). We therefore attribute the ~ 144 K shifting of the Bi_h TL peak towards lower temperature to the decreased activation energy for hole liberation from Bi^{4+} with increasing y in $\text{LiLu}_{0.25}\text{Y}_{0.75}\text{Si}_{1-y}\text{Ge}_y\text{O}_4:0.01\text{Bi}^{3+}$. The results in columns 2 and 3 of Table 2 demonstrate that the TLE maximum coincides with the $\text{Bi}^{3+} \rightarrow \text{CB}$ D-band. The Bi^{3+} D-band energies were used to place the ground state levels of Bi^{3+} below the CB bottom in Fig. 1a) and b). During Bi^{3+} D-band excitation, electrons from the $^1\text{S}_0$ ground state of Bi^{3+} are excited to the conduction band, which then can be captured by electron traps like the Bi^{3+} and Sm^{3+} in Fig. 7a)-c) or other host-related electron traps like those responsible for the TL glow peak at about 354, 452, and 559 K in Fig. S18c), and Bi^{4+} remains.

The result in Fig. 6a) also implies that one can design Bi^{3+} based storage phosphors in $\text{LiLu}_{0.25}\text{Y}_{0.75}\text{Si}_{1-y}\text{Ge}_y\text{O}_4:0.01\text{Bi}^{3+}$ by engineering the Bi^{3+} hole trap depth through changing the ratio of silicon to germanium. With increasing silicon content, the TL peak shifts from 371 K to 538 K, which is consistent with the decrease of the Bi^{3+} persistent luminescence in Fig. 6b) and the less TL fading in Fig. 6c). With further crystal synthesis optimization, a good storage phosphor may appear like $\text{LiLu}_{0.25}\text{Y}_{0.75}\text{SiO}_4:0.01\text{Bi}^{3+}$ in Fig. 8a) in which the integrated TL intensity between 300 and 800 K is about 4.4 times higher than that of commercial $\text{BaFBr}(\text{I}):\text{Eu}^{2+}$ phosphor after β irradiation.

4.4. Information storage application using Ce^{3+} and Bi^{3+} storage phosphors

The TL excitation spectra in Fig. S13c) show that the Ce^{3+} 4f-5d₁ excitation band near 350 nm can charge the $\text{LiLuSiO}_4:0.01\text{Ce}^{3+},0.01\text{Sm}^{3+}$. It implies that $\text{LiLu}_{1-x}\text{Y}_x\text{SiO}_4:0.01\text{Ce}^{3+},0.01\text{Sm}^{3+}$ when applied as a storage phosphor needs to be kept in the dark during X-ray exposure. For the Bi^{3+} -doped $\text{LiLu}_{1-x}\text{Y}_x\text{SiO}_4$ in Fig. 5c) and $\text{LiLu}_{0.25}\text{Y}_{0.75}\text{Si}_{1-y}\text{Ge}_y\text{O}_4$ in Fig. 6a), only the Bi^{3+} D-band near 210–230 nm can fill the traps. This means that such Bi^{3+} -based storage phosphor can be kept in daylight during X-ray exposure.

The TL emission spectra in Fig. S3) show that the thermally stimulated Ce^{3+} 5d-4f emission which has ~ 39 ns fluorescence decay time in Fig. S25 appears in the visible region, while the Bi^{3+} A-band emission peaking near 360 nm in Fig. 3e) with ~ 0.5 μs fluorescence decay time in Fig. S26–S27 emerges largely in the ultraviolet region. Both thermally stimulated Ce^{3+} and Bi^{3+} emissions in $\text{LiLu}_{1-x}\text{Y}_x\text{SiO}_4$ phosphors match well with a traditional photomultiplier tube and are quite intense compared with the commercial $\text{BaFBr}(\text{I}):\text{Eu}^{2+}$ storage phosphor in Fig. 8a). This combined with better TL fading characteristics in Fig. 8c) and the photon stimulation ability of the charge carriers stored during β -ray exposure in Fig. 9 indicates that the developed phosphors have potential application as optically stimulated storage phosphors for information storage as demonstrated in Fig. 10 and S29–S31.

5. Conclusions

The methodology to rational design of storage phosphors with high charge carrier storage capacity for information storage has been explored by studying both the trapping and detrapping processes of electrons and holes in the bismuth and lanthanide-doped $\text{LiRE}(\text{Si},\text{Ge})\text{O}_4$

(RE = Y, Lu) family of compounds. For $\text{LiLuSiO}_4:0.01\text{Ln}^{3+}, 0.01\text{Tm}^{3+}$ (Ln = Ce, Pr, or Tb) and $\text{LiLuSiO}_4:0.01\text{Bi}^{3+}, 0.01\text{Tm}^{3+}$, the Tm^{3+} acts as an electron trap, while the Ln^{3+} and Bi^{3+} codopants are the hole traps and recombination centres. The electrons are released from Tm^{2+} to recombine with holes captured at Ln^{4+} and Bi^{4+} to generate characteristic Ln^{3+} 4f-4f or 5d-4f emission and Bi^{3+} A-band emission. The electron trap depth can be controlled by the choice of Tm^{3+} or Sm^{3+} codopant, and for fixed pair of Bi^{3+} and/or Ln^{3+} dopants like in $\text{LiLu}_{1-x}\text{Y}_x\text{SiO}_4:0.01\text{Ce}^{3+}, 0.01\text{Ln}^{3+}$ (Ln = Tm or Sm) and $\text{LiLu}_{1-x}\text{Y}_x\text{SiO}_4:0.01\text{Bi}^{3+}, 0.01\text{Sm}^{3+}$ solid solutions, by changing x, resulting in conduction band engineering. The integrated TL intensity of the optimized $\text{LiLu}_{0.5}\text{Y}_{0.5}\text{SiO}_4:0.01\text{Ce}^{3+}, 0.005\text{Sm}^{3+}$ is about 8.5 times higher than that of the commercial $\text{BaFBr}(\text{I}):\text{Eu}^{2+}$ storage phosphor after β irradiation. In $\text{LiLuSiO}_4: 0.01\text{Eu}^{3+}, 0.01\text{Ln}^{3+}$ (Ln = Tb or Pr), $\text{LiLuSiO}_4:0.01\text{Eu}^{3+}, 0.01\text{Bi}^{3+}$, and $\text{LiLuSiO}_4:0.01\text{Bi}^{3+}$, the Eu^{3+} and Bi^{3+} act as the deep electron traps and recombination centres, while Tb^{3+} , Pr^{3+} , and Bi^{3+} act as the less deep hole traps. The holes are liberated from Tb^{4+} , Pr^{4+} , and Bi^{4+} to recombine with electrons at Eu^{2+} and Bi^{2+} to produce typical Eu^{3+} 4f-4f and Bi^{3+} A-band emissions. The hole trap depth can be controlled by the choice of Tb^{3+} , Pr^{3+} , and Bi^{3+} , and for the fixed pair of Ln^{3+} and/or Bi^{3+} like in $\text{LiLu}_{1-x}\text{Y}_x\text{SiO}_4:0.01\text{Eu}^{3+}, 0.01\text{Ln}^{3+}$ (Ln = Tb or Pr), $\text{LiLu}_{1-x}\text{Y}_x\text{SiO}_4:0.01\text{Eu}^{3+}, 0.01\text{Bi}^{3+}$, and $\text{LiLu}_{1-x}\text{Y}_x\text{SiO}_4:0.01\text{Bi}^{3+}$, by tailoring x, resulting in valence band engineering. The VRBE at the CB-bottom and VB-top can be engineered by replacing Si^{4+} for Ge^{4+} in $\text{LiLu}_{0.25}\text{Y}_{0.75}\text{Si}_{1-y}\text{Ge}_y\text{O}_4:0.01\text{Bi}^{3+}$, leading to the tailoring of Bi^{3+} hole trap depth. The TL intensity of the optimized $\text{LiLu}_{0.25}\text{Y}_{0.75}\text{SiO}_4:0.01\text{Bi}^{3+}$ is ~ 4.4 times higher than that of the commercial $\text{BaFBr}(\text{I}):\text{Eu}^{2+}$. Proof-of-concept information storage was demonstrated with X-ray or UV-light charged $\text{LiLu}_{0.5}\text{Y}_{0.5}\text{SiO}_4:0.01\text{Ce}^{3+}, 0.01\text{Sm}^{3+}$ and $\text{LiLu}_{0.25}\text{Y}_{0.75}\text{SiO}_4:0.01\text{Bi}^{3+}$ phosphors dispersed in silicone gel imaging plates. This paper not only reports excellent Ce^{3+} and Bi^{3+} based storage phosphors but more importantly demonstrates a feasible strategy to discover Ce^{3+} and Bi^{3+} based storage phosphors based on tailoring trapping, detrapping, and recombination processes of both electrons and holes. This work can also inspire future research to develop Ce^{3+} and Bi^{3+} based storage phosphors for energy storage in a rational design approach rather than using a trial-and-error method.

Acknowledgements

T. Lyu acknowledges the China Scholarship Council for his PhD scholarship (Tianshuai Lyu: No. 201608320151).

Declaration of interests

The authors declare that they have no known competing financial interests or personal relationships that could have appeared to influence the work reported in this paper.

Appendix A. Supplementary data

Supplementary data to this article can be found online at <https://doi.org/10.1016/j.cej.2020.124776>.

References

- Y. Li, M. Gecevicius, J. Qiu, Long persistent phosphors—from fundamentals to applications, *Chem. Soc. Rev.* 45 (2016) 2090–2136.
- H. Luo, A.J.J. Bos, P. Dorenbos, Controlled electron-hole trapping and detrapping process in GdAlO_3 by valence band engineering, *J. Phys. Chem. C* 120 (2016) 5916–5925.
- J. Xu, S. Tanabe, Persistent luminescence instead of phosphorescence: history, mechanism, and perspective, *J. Lumin.* 205 (2019) 581–620.
- J. Ueda, J.L. Leano, C. Richard, K. Asami, S. Tanabe, R.-S. Liu, Broadband near-infrared persistent luminescence of $\text{Ba}[\text{Mg}_2\text{Al}_2\text{N}_4]$ with Eu^{2+} and Tm^{3+} after red light charging, *J. Mater. Chem. C* 7 (2019) 1705–1712.
- J. Ueda, P. Dorenbos, A.J.J. Bos, K. Kuroishi, S. Tanabe, Control of electron transfer between Ce^{3+} and Ce^{3+} in the $\text{Y}_3\text{Al}_{5-x}\text{Ga}_x\text{O}_{12}$ host via conduction band engineering, *J. Mater. Chem. C* 3 (2015) 5642–5651.
- Y. Zhuang, Y. Lv, Y. Li, T. Zhou, J. Xu, J. Ueda, S. Tanabe, R.-J. Xie, Study on trap levels in $\text{SrSi}_2\text{AlO}_2\text{N}_3:\text{Eu}^{2+}, \text{Ln}^{3+}$ persistent phosphors based on host-referred binding energy scheme and thermoluminescence analysis, *Inorg. Chem.* 55 (2016) 11890–11897.
- T. Wang, W. Bian, D. Zhou, J. Qiu, X. Yu, X. Xu, Tunable LLP via energy transfer between $\text{Na}_{2-y}(\text{Zn}_{1-x}\text{Ga}_x)\text{GeO}_4$ spheruloid host and emission centers with the assistance of Zn vacancies, *J. Phys. Chem. C* 119 (2015) 14047–14055.
- S. Wang, X. Liu, B. Qu, Z. Song, Z. Wang, S. Zhang, F. Wang, W.-T. Geng, Q. Liu, Green persistent luminescence and the electronic structure of β - $\text{SiAlon}:\text{Eu}^{2+}$, *J. Mater. Chem. C* 7 (2019) 12544–12551.
- K. Korthout, K. Van den Eckhout, J. Botterman, S. Nikitenko, D. Poelman, P.F. Smet, Luminescence and x-ray absorption measurements of persistent $\text{SrAl}_2\text{O}_4:\text{Eu}$, Dy powders: evidence for valence state changes, *Phys. Rev. B* 84 (2011) 085140.
- J. Ueda, M. Katayama, K. Asami, J. Xu, Y. Inada, S. Tanabe, Evidence of valence state change of Ce^{3+} and Cr^{3+} during UV charging process in $\text{Y}_3\text{Al}_2\text{Ga}_3\text{O}_{12}$ persistent phosphors, *Opt. Mater. Express* 7 (2017) 2471–2476.
- H. Luo, A.J.J. Bos, P. Dorenbos, Charge carrier trapping processes in $\text{RE}_2\text{O}_2\text{S}$ (RE = La, Gd, Y, and Lu), *J. Phys. Chem. C* 121 (2017) 8760–8769.
- K. Chakrabarti, V.K. Mathur, J.F. Rhodes, R.J. Abbundi, Stimulated luminescence in rare-earth-doped MgS, *J. Appl. Phys.* 64 (1988) 1363–1366.
- T. Lyu, P. Dorenbos, Charge carrier trapping processes in lanthanide doped LaPO_4 , GdPO_4 , YPO_4 , and LuPO_4 , *J. Mater. Chem. C* 6 (2018) 369–379.
- T. Lyu, P. Dorenbos, Bi^{3+} acting both as an electron and as a hole trap in La-, Y-, and LuPO_4 , *J. Mater. Chem. C* 6 (2018) 6240–6249.
- T. Lyu, P. Dorenbos, Designing thermally stimulated $1.06 \mu\text{m}$ Nd^{3+} emission for the second bio-imaging window demonstrated by energy transfer from Bi^{3+} in La-, Gd-, Y-, and LuPO_4 , *Chem. Eng. J.* 372 (2019) 978–991.
- H.-T. Sun, J. Zhou, J. Qiu, Recent advances in bismuth activated photonic materials, *Prog. Mater. Sci.* 64 (2014) 1–72.
- X. Wang, P. Boutinaud, L. Li, J. Cao, P. Xiong, X. Li, H. Luo, M. Peng, Novel persistent and tribo-luminescence from bismuth ion pairs doped strontium gallate, *J. Mater. Chem. C* 6 (2018) 10367–10375.
- H. Luo, P. Dorenbos, The dual role of Cr^{3+} in trapping holes and electrons in lanthanide co-doped GdAlO_3 and LaAlO_3 , *J. Mater. Chem. C* 6 (2018) 4977–4984.
- R.H.P. Awater, P. Dorenbos, The Bi^{3+} 6s and 6p electron binding energies in relation to the chemical environment of inorganic compounds, *J. Lumin.* 184 (2017) 221–231.
- R.H.P. Awater, L.C. Niemeijer-Berghuis, P. Dorenbos, Luminescence and charge carrier trapping in $\text{YPO}_4:\text{Bi}$, *Opt. Mater.* 66 (2017) 351–355.
- P. Dorenbos, A review on how lanthanide impurity levels change with chemistry and structure of inorganic compounds, *ECS J. Solid State Sci. Technol.* 2 (2013) R3001–R3011.
- P. Dorenbos, Modeling the chemical shift of lanthanide 4f electron binding energies, *Phys. Rev. B* 85 (2012) 165107.
- J. Ueda, S. Tanabe, (INVITED) Review of luminescent properties of Ce^{3+} -doped garnet phosphors: New insight into the effect of crystal and electronic structure, *Opt. Mater.: X* 1 (2019) 100018.
- J. Ueda, R. Maki, S. Tanabe, Vacuum referred binding energy (VRBE)-guided design of orange persistent $\text{Ca}_3\text{Si}_2\text{O}_7:\text{Eu}^{2+}$ phosphors, *Inorg. Chem.* 56 (2017) 10353–10360.
- H. Luo, A.J.J. Bos, A. Dobrowolska, P. Dorenbos, Low-temperature VUV photoluminescence and thermoluminescence of UV excited afterglow phosphor $\text{Sr}_3\text{Al}_2\text{Si}_5\text{O}_{15}:\text{Ce}^{3+}, \text{Ln}^{3+}$ (Ln = Er, Nd, Sm, Dy and Tm), *Phys. Chem. Chem. Phys.* 17 (2015) 15419–15427.
- Z. Wang, Z. Song, L. Ning, Q. Liu, Sunlight-activated yellow long persistent luminescence from Nb-doped $\text{Sr}_3\text{SiO}_5:\text{Eu}^{2+}$ for warm-color mark applications, *J. Mater. Chem. C* 8 (2020) 1143–1150.
- M. Gu, Q. Zhang, S. Lamon, Nanomaterials for optical data storage, *Nat. Rev. Mater.* 1 (2016) 16070.
- X. Huang, Q. Guo, D. Yang, X. Xiao, X. Liu, Z. Xia, F. Fan, J. Qiu, G. Dong, Reversible 3D laser printing of perovskite quantum dots inside a transparent medium, *Nat. Photon.* 14 (2020) 82–88.
- Y. Zhuang, L. Wang, Y. Lv, T.-L. Zhou, R.-J. Xie, Optical data storage and multicolor emission readout on flexible films using deep-trap persistent luminescence materials, *Adv. Funct. Mater.* 28 (2018) 1705769.
- M. Gu, X. Li, Y. Cao, Optical storage arrays: a perspective for future big data storage, *Light Sci. Appl.* 3 (2014) e177.
- D. Genovese, A. Aliprandi, E.A. Prasetyanto, M. Mauro, M. Hirtz, H. Fuchs, Y. Fujita, H. Uji-i, S. Lebedkin, M. Kappes, L. De Cola, Mechano- and photochromism from bulk to nanoscale: data storage on individual self-assembled ribbons, *Adv. Funct. Mater.* 26 (2016) 5271–5278.
- H. Sun, S. Liu, W. Lin, K.Y. Zhang, W. Lv, X. Huang, F. Huo, H. Yang, G. Jenkins, Q. Zhao, W. Huang, Smart responsive phosphorescent materials for data recording and security protection, *Nat. Commun.* 5 (2014) 3601.
- S. Hirata, K.-S. Lee, T. Watanabe, Reversible fluorescent on-off recording in a highly transparent polymeric material utilizing fluorescent resonance energy transfer (FRET) induced by heat treatment, *Adv. Funct. Mater.* 18 (2008) 2869–2879.
- B.H. Cumpston, S.P. Ananthavel, S. Barlow, D.L. Dyer, J.E. Ehrlich, L.L. Erskine, A.A. Heikal, S.M. Kuebler, I.Y.S. Lee, D. McCord-Maughon, J. Qin, H. Röckel, M. Rumi, X.-L. Wu, S.R. Marder, J.W. Perry, Two-photon polymerization initiators for three-dimensional optical data storage and microfabrication, *Nature* 398 (1999) 51–54.

- [35] A. Dobrowolska, A.J.J. Bos, P. Dorenbos, High charge carrier storage capacity in lithium lutetium silicate doped with cerium and thulium, *Physica Status Solidi* 13 (2019) 1800502.
- [36] M. Thoms, H. von Seggern, A. Winnacker, Spatial correlation and photostimulability of defect centers in the x-ray-storage phosphor BaFBr:Eu²⁺, *Phys. Rev. B* 44 (1991) 9240–9247.
- [37] Y. Gao, R. Li, W. Zheng, X. Shang, J. Wei, M. Zhang, J. Xu, W. You, Z. Chen, X. Chen, Broadband NIR photostimulated luminescence nanoprobe based on CaS:Eu²⁺, Sm³⁺ nanocrystals, *Chem. Sci.* 10 (2019) 5452–5460.
- [38] H. Shi, Z. An, Ultraviolet afterglow, *Nat. Photon.* 13 (2019) 74–75.
- [39] Y.-M. Yang, Z.-Y. Li, J.-Y. Zhang, Y. Lu, S.-Q. Guo, Q. Zhao, X. Wang, Z.-J. Yong, H. Li, J.-P. Ma, Y. Kuroiwa, C. Moriyoshi, L.-L. Hu, L.-Y. Zhang, L.-R. Zheng, H.-T. Sun, X-ray-activated long persistent phosphors featuring strong UVC afterglow emissions, *Light Sci. Appl.* 7 (2018) 88.
- [40] S. Lin, H. Lin, C. Ma, Y. Cheng, S. Ye, F. Lin, R. Li, J. Xu, Y. Wang, High-security-level multi-dimensional optical storage medium: nanostructured glass embedded with LiGa₂O₅: Mn²⁺ with photostimulated luminescence, *Light Sci. Appl.* 9 (2020) 22.
- [41] S. Lin, H. Lin, Q. Huang, Y. Cheng, J. Xu, J. Wang, X. Xiang, C. Wang, L. Zhang, Y. Wang, A photostimulated BaSi₂O₅:Eu²⁺, Nd³⁺ phosphor-in-glass for erasable-rewritable optical storage medium, *Laser Photon. Rev.* (2019) 1900006.
- [42] W. Li, Y. Zhuang, P. Zheng, T.-L. Zhou, J. Xu, J. Ueda, S. Tanabe, L. Wang, R.-J. Xie, Tailoring trap depth and emission wavelength in Y₃Al_{5-x}Ga_xO₁₂:Ce³⁺, V³⁺ phosphor-in-glass films for optical information storage, *ACS Appl. Mater. Interfaces* 10 (2018) 27150–27159.
- [43] C. Wang, Y. Jin, Y. Lv, G. Ju, D. Liu, L. Chen, Z. Li, Y. Hu, Trap distribution tailoring guided design of super-long-persistent phosphor Ba₂SiO₄:Eu²⁺, Ho³⁺ and photostimulable luminescence for optical information storage, *J. Mater. Chem. C* 6 (2018) 6058–6067.
- [44] Z. Liu, L. Zhao, W. Chen, X. Fan, X. Yang, S. Tian, X. Yu, J. Qiu, X. Xu, Multiple anti-counterfeiting realized in NaBaScSi₂O₇ with a single activator of Eu²⁺, *J. Mater. Chem. C* 6 (2018) 11137–11143.
- [45] P. Leblans, D. Vandebroucke, P. Willems, Storage phosphors for medical imaging, *Materials* 4 (2011) 1034.
- [46] C. Chen, Y. Zhuang, D. Tu, X. Wang, C. Pan, R.-J. Xie, Creating visible-to-near-infrared mechanoluminescence in mixed-anion compounds SrZn₂S₂O and SrZnSO, *Nano Energy* 68 (2020) 104329.
- [47] A. Bedard, T.D. Davis, C. Angelopoulos, Storage phosphor plates: how durable are they as a digital dental radiographic system, *J. Contemp. Dent. Pract.* 5 (2004) 57–69.
- [48] K. Takahashi, K. Kohda, J. Miyahara, Y. Kanemitsu, K. Amitani, S. Shionoya, Mechanism of photostimulated luminescence in BaFX:Eu²⁺ (X = Cl, Br) phosphors, *J. Lumin.* 31–32 (1984) 266–268.
- [49] S. Schweizer, L.W. Hobbs, M. Secu, J.-M. Spaeth, A. Edgar, G.V.M. Williams, Photostimulated luminescence in Eu-doped fluorochlorozirconate glass ceramics, *Appl. Phys. Lett.* 83 (2003) 449–451.
- [50] G.A. Appleby, J. Zimmermann, S. Hesse, O. Karg, H.v. Seggern, Sensitization of the photostimulable x-ray storage-phosphor CsBr:Eu²⁺ following room-temperature hydration, *J. Appl. Phys.* 105 (2009).
- [51] H. Vrielinck, F. Loncke, J.P. Tahon, P. Leblans, P. Matthys, F. Callens, Electron nuclear double resonance study of photostimulated luminescence active centers in CsBr:Eu²⁺ medical imaging plates, *Phys. Rev. B* 83 (2011) 054102.
- [52] D. Kulesza, P. Bolek, A.J.J. Bos, E. Zych, Lu₂O₃-based storage phosphors. An (in) harmonious family, *Coord. Chem. Rev.* 325 (2016) 29–40.
- [53] A.V. Sidorenko, P. Dorenbos, A.J.J. Bos, C.W.E. van Eijk, P.A. Rodnyi, Lanthanide level location and charge carrier trapping in LiLnSiO₄: Ce³⁺, Sm³⁺, Ln = Y or Lu, *J. Phys.-Condens. Matter* 18 (2006) 4503–4514.
- [54] A. Dobrowolska, A.J.J. Bos, P. Dorenbos, Synthesis optimization and charge carrier transfer mechanism in LiLuSiO₄:Ce, Tm storage phosphor, *Rad. Meas.* 127 (2019) 106147.
- [55] T. Lyu, P. Dorenbos, Vacuum referred binding energies of bismuth and lanthanide levels in ARE(Si,Ge)O₄ (A = Li, Na; RE = Y, Lu); towards designing charge carrier trapping processes for energy storage, *Chem. Mater.* 32 (2020) 1192–1209.
- [56] A.J.J. Bos, R.M. van Duijvenvoorde, E. van der Kolk, W. Drozdowski, P. Dorenbos, Thermoluminescence excitation spectroscopy: a versatile technique to study persistent luminescence phosphors, *J. Lumin.* 131 (2011) 1465–1471.
- [57] W. Hoogenstraaten, Electron traps in zinc-sulphide phosphors, *Philips Res. Rep.* 13 (1958) 515–693.
- [58] R. Chen, S.A.A. Winer, Effects of Various Heating Rates on Glow Curves, *J. Appl. Phys.* 41 (1970) 5227–5232.
- [59] J. Azorin, Determination of thermoluminescence parameters from glow curves—I. A review, *Int. J. Rad. Appl. Instrum. Part D* 11 (1986) 159–166.
- [60] P. Dorenbos, Charge transfer bands in optical materials and related defect level location, *Opt. Mater.* 69 (2017) 8–22.
- [61] P.W. Tasker, A.M. Stoneham, An appraisal of the molecular model for the V_k centre, *J. Phys. Chem. Solids* 38 (1977) 1185–1189.
- [62] R.B. Murray, F.J. Keller, Recombination luminescence from V_k centers in potassium iodide, *Phys. Rev.* 137 (1965) A942–A948.
- [63] R. Gazzinelli, G.M. Ribeiro, M.L. de Siqueira, ESR and endor studies of the V_k center in SrF₂, *Solid State Commun.* 13 (1973) 1131–1134.
- [64] N.F. Mott, A.M. Stoneham, The lifetime of electrons, holes and excitons before self-trapping, *J. Phys. C: Solid State Phys.* 10 (1977) 3391.
- [65] P. Dorenbos, The Pr³⁺ and Tb³⁺ ground state locations in compounds obtained from thermoluminescence and intervalence charge transfer studies, *Opt. Mater.* 91 (2019) 333–337.
- [66] P. Dorenbos, The nephelauxetic effect on the electron binding energy in the 4f_q ground state of lanthanides in compounds, *J. Lumin.* 214 (2019) 116536.